

2

AD-A262 956

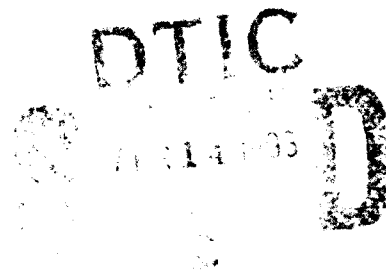


NAWCWPNS TP 8103

Fractional Brownian Motion, Wavelets, and Infrared Detector Noise

by
G. A. Hewer
and
Wei Kuo
Intercept Weapons Department

MARCH 1993



NAVAL AIR WARFARE CENTER WEAPONS DIVISION
China Lake, CA 93555-6001



Approved for public release;
distribution is unlimited.

93 4 18 034

93-07696

73

Naval Air Warfare Center Weapons Division

FOREWORD

The purpose of this report is to summarize our joint research on fractional Brownian motion, wavelets, and infrared detector noise. The report presents the hypothesis that fractional Brownian motion is a good approximate model for the detector noise present on infrared staring arrays when they are imaging a uniform background. The work was done at the Naval Air Warfare Center Weapons Division, China Lake, Calif., during 1992 under Program Element Task Area RA11C12, Work Units 129295.

This report was reviewed for technical accuracy by Dr. Brett Borden.

Approved by
DR. J. A. WUNDERLICH, *Head*
Intercept Weapons Department
17 March 1993

Under authority of
W. E. NEWMAN
RAdm., U.S. Navy
Commander

Released for publication by
S. HAALAND
Deputy Commander for Research & Development

NAWCWPNS Technical Publication 8103

Published by Technical Information Department
Collation Cover, 35 leaves
First printing 100 copies

REPORT DOCUMENTATION PAGE

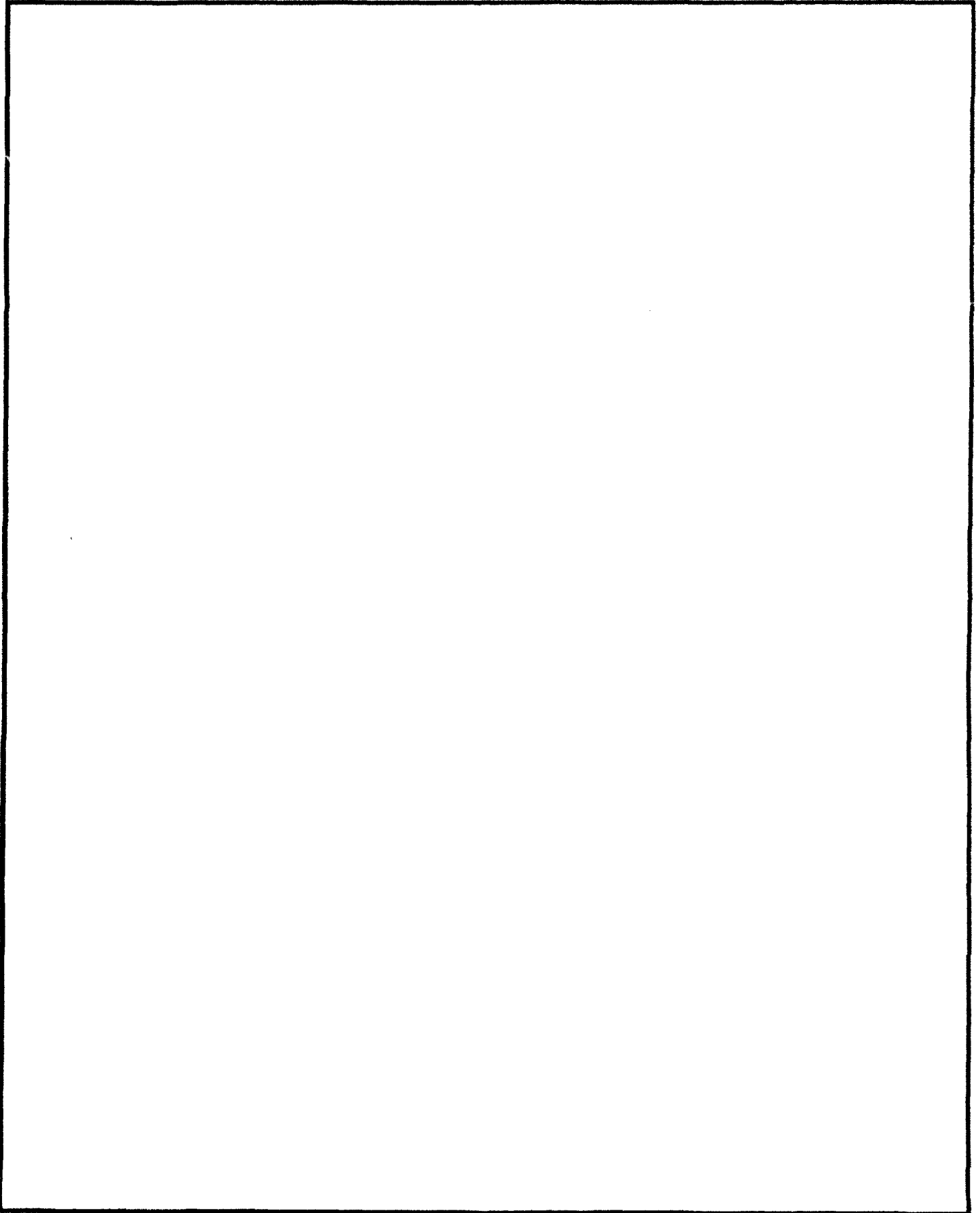
Form Approved
OMB No. 0704-0188

Public reporting burden for this collection of information is estimated to average 1 hour per response, including the time for reviewing instructions, searching existing data sources, gathering and maintaining the data needed, and completing and reviewing the collection of information. Send comments regarding this burden estimate or any other aspect of this collection of information, including suggestions for reducing this burden, to Washington Headquarters Services, Directorate for Information Operations and Reports, 1215 Jefferson Davis Highway, Suite 1204, Arlington, VA 22202-4302, and to the Office of Management and Budget, Paperwork Reduction Project (0704-0188), Washington, DC 20503.

| | | | | |
|--|---|--|---|--|
| 1. AGENCY USE ONLY (Leave blank) | | 2. REPORT DATE March 1993 | 3. REPORT TYPE AND DATES COVERED Final | |
| 4. TITLE AND SUBTITLE Fractional Brownian Motion, Wavelets, and Infrared Detector Noise | | | 5. FUNDING NUMBERS | |
| 6. AUTHOR(S) G. A. Hewer and Wei Kuo | | | | |
| 7. PERFORMING ORGANIZATION NAME(S) AND ADDRESS(ES) Naval Air Warfare Center Weapons Division China Lake, CA 93555-6001 | | | 8. PERFORMING ORGANIZATION REPORT NUMBER NAWCWPNS TP 8103 | |
| 9. SPONSORING/MONITORING AGENCY NAME(S) AND ADDRESS(ES) | | | 10. SPONSORING/MONITORING AGENCY REPORT NUMBER | |
| 11. SUPPLEMENTARY NOTES | | | | |
| 12A. DISTRIBUTION/AVAILABILITY STATEMENT Approved for public release; distribution is unlimited. | | | 12B. DISTRIBUTION CODE | |
| 13. ABSTRACT (Maximum 200 words) Fractional Brownian motion (fBm) is the proper model for spatial noise. The noise on infrared arrays has both a temporal and a spatial component. Spatial noise (pixel-to-pixel variation) manifests itself across the array as a nonuniform response by the individual detectors to a uniform illumination. Temporal noise is observed by sampling the time series response from a single pixel. In this report the pixel responses from an indium antimonide (InSb) staring array are analyzed for their 1/f characteristics. | | | | |
| 14. SUBJECT TERMS Fractional Brownian motion infrared detector noise staring focal plane array wavelets | | | 15. NUMBER OF PAGES 67 | |
| | | | 16. PRICE CODE | |
| 17. SECURITY CLASSIFICATION OF REPORT UNCLASSIFIED | 18. SECURITY CLASSIFICATION OF THIS PAGE UNCLASSIFIED | 19. SECURITY CLASSIFICATION OF ABSTRACT UNCLASSIFIED | 20. LIMITATION OF ABSTRACT | |

UNCLASSIFIED

SECURITY CLASSIFICATION OF THIS PAGE (When Data Entered)



CONTENTS

| | |
|---------------------------------------|----|
| Introduction | 3 |
| FBm, Wavelets, and ARIMA Models | 6 |
| FBm Simulation and Examples | 19 |
| Amber Camera Test Results | 27 |
| Conclusions | 32 |
| References | 65 |

| | |
|---------------|--------------|
| Accession For | |
| NTIS | CRAB |
| DTIC | 145 |
| Unannounced | |
| Justification | |
| By | |
| Date | |
| Approved For | |
| Dist. | Approved For |
| | Spec |
| A-1 | |

Figures:

| | |
|--|----|
| 1. Fast Wavelet Transform Block Diagram | 13 |
| 2. FBms and Their Periodograms | 35 |
| 3. FBms and Their Autocorrelation Functions | 36 |
| 4. Increments of FBms and Their Correlation Functions | 37 |
| 5. Scale and Wavelet Functions of Several Wavelets | 38 |
| 6. FBm With $d = 0.4$ and Haar Wavelet | 39 |
| 7. FBm With $d = -0.4$ and Haar Wavelet | 40 |
| 8. FBm With $d = 0.4$ and Daubechies 10 Wavelet | 41 |
| 9. FBm With $d = -0.4$ and Daubechies 10 Wavelet | 42 |
| 10. Estimation of H of fBm With $d = 0.4$ ($H = 0.9$) by Hurst Rescaled Range and Daubechies 10 Wavelet | 43 |
| 11. Estimation of H of fBm With $d = 0.4$ ($H = 0.9$) by Hurst Rescaled Range and Daubechies 10 Wavelet | 44 |
| 12. Estimation of H of fBm With $d = -0.4$ ($H = 0.1$) by Daubechies 10 and Mixed Daubechies Wavelets | 45 |
| 13. Sensitivity of fBm to Noise | 46 |
| 14. Normal Q-Q Plots and Variance Step Size Effect | 47 |
| 15. Histograms and Estimated Probability Density Functions of fBms and Their Increments | 48 |
| 16. Correlation Functions Between fBms With $d = -0.3$ | 49 |
| 17. Correlation Functions Between Increments of fBm With $d = -0.3$ | 50 |

Figures (contd.):

| | | |
|-----|--|----|
| 18. | Decomposition and Reconstruction of fBm Using Daubechies 10 Wavelet | 51 |
| 19. | Comparison of the Estimated H for a Short-Term and a Long-Term fBm | 52 |
| 20. | Power Spectrums for Amber Camera Data and Their Spline Fits | 53 |
| 21. | Long-Term Amber Camera Data and Their Periodograms | 54 |
| 22. | Amber Camera Data and Their Normal Q-Q Plots | 55 |
| 23. | Histograms and Estimated Probability Density Functions of Long-Term Amber Camera Data | 56 |
| 24. | Comparison of the Estimated H for Long-Term Amber Camera Data | 57 |
| 25. | Correlation Functions Between Long-Term Amber Camera Data Pixel (10,10) and Pixel (10,11) | 58 |
| 26. | Correlation Functions Between Long-Term Amber Camera Data Pixel (10,10) and Pixel (10,11) | 59 |
| 27. | 54-Hertz Amber Camera Data and Their Periodograms | 60 |
| 28. | 54-Hertz Amber Camera Data and Their Normal Q-Q Plots | 61 |
| 29. | Histograms and Estimated Probability Density Functions of 54-Hertz Amber Camera Data | 62 |
| 30. | 54-Hertz Amber Camera Data and Haar Wavelet | 63 |
| 31. | 54-Hertz Amber Camera Data and Daubechies 10 Wavelet | 64 |

Tables:

| | | |
|----|--|----|
| 1. | Comparative Statistics for the Estimation of the Index H | 21 |
| 2. | Comparative Statistics for the Estimation of the Index H | 22 |
| 3. | Camera Parameter Settings | 28 |
| 4. | Fourier Sampling Parameters | 28 |
| 5. | Amber Camera Statistics | 30 |
| 6. | Amber Camera Global Statistics | 31 |

ACKNOWLEDGMENT

The authors would like to thank Keel Anthony, Dr. Dave Kyser, and Douglas Lamb for assistance with the Amber infrared camera measurements. Without their valuable skill and time the necessary measurements for the hypothesis testing and validation section of this report would have been unavailable.

INTRODUCTION

In this report the pixel responses from an indium antimonide (InSb) staring array are analyzed for their $1/f$ characteristics. The InSb array has a spectral band of 3 to 5.5 micrometers (μm). Examples of the test data, the tabulated values, and the camera parameters are presented later in the Amber Camera Test Results section.

The basic hypothesis presented in this report is that fractional Brownian motion (fBm) is the proper model for spatial noise. The emphasis in this report is on fBm, wavelets, and statistics. The interested reader can consult the reports of Scribner and others (References 1 through 4) and the references therein to find further discussion of detector physics and supporting periodogram spectral plots that clearly exhibit a $1/f$ -type characteristic on the arrays studied. Although the definitive work on the physics of $1/f$ noise has apparently not been written, a body of literature exists that offers physical theory for the presence of $1/f$ noise in detectors (Reference 5).

The noise on infrared arrays has both a temporal and a spatial component (Reference 6). Spatial noise (pixel-to-pixel variation) manifests itself across the array as a nonuniform response by the individual detectors to a uniform illumination. Temporal noise is observed by sampling the time series response from a single pixel. According to Silverman and others, temporal noise results from the "randomness inherent in the arrival and detection of infrared photons." "The magnitude of temporal noise increases as the square root of the measurement time, whereas the magnitude of the signal increases linearly" (Reference 6).

Scribner and others in a series of papers have investigated the $1/f$ character of fixed pattern noise in staring arrays (References 1 through 4). According to these investigators, "Two sources of spatial noise after nonuniformity correction are $1/f$ noise and pixel nonlinearities" (Reference 2). For example, the report exhibits spectral plots for mercury cadmium telluride (HgCdTe) staring arrays that show a spectrum with a $1/f$ -type noise characteristic in the lower frequency band and with a white-noise spectrum in the remaining frequency band. The plots also show that platinum silicide (PtSi) arrays have a spectrum that is mostly white. The HgCdTe had a frame rate of 60 Hertz with a spectral band of 4.33 to 4.9 μm , and the rate for the PtSi 3.6- to 4.3- μm array was 30 Hertz. This report is not the place for a detailed review; the reader interested in the details is referred to References 1 through 4.

Noise having a power spectrum that is inversely proportional to the inverse of the frequency (i.e., f^{-1}) is classic $1/f$ -type noise and is sometimes called pink noise. It has equal power in octave frequency bands. Flicker noise or $1/f$ -type noise is often identified

by a -1 decade per decade asymptotic slope, which it produces on a log-log plot of the power spectrum—specifically, the periodogram. Pink noise is encountered in a wide variety of physical systems, including semiconductor devices. The papers by West and Shlesinger (Reference 7) and Montroll and Shlesinger (Reference 8) present highly readable introductions to the classic $1/f$ noise. Noise having a power spectrum that is inversely proportional to the inverse square of the frequency (i.e., f^{-2}) is called brown noise in an allusion to Brownian motion. Black noise has a power spectrum that is inversely proportional to some power—for example, α of the frequency—where the power law exponent is greater than two. Black noise is beyond brown noise. All these different colored noises whose power spectrums are inversely proportional to some inverse power α of the frequency (i.e., $f^{-\alpha}$ for $1 < \alpha < 3$) are examples of $1/f$ -type noise processes. White noise has a flat spectrum over some finite range of frequencies. For a lively and intriguing discussion of these colored noises, see the book *Fractals, Chaos, Power Laws* (Reference 9).

Implicit in the discussion of $1/f$ processes is the fact that they have a well-defined spectrum. The theory of flicker noise is delicate and far from trivial, because the frequency spectrum f^{-1} is not integrable on the semi-infinite interval $(0, \infty)$, which suggests infinite variance and therefore that the spectrum of the process apparently cannot exist. Normally these characterizations come from stochastic process theory. Stochastic process theory provides a dynamic mathematical theory of random events that occur in time or space. Recently Solo has addressed the nonintegrability issue of the $1/f$ spectrum; namely, he has rigorously established “An explicit definition of the spectrum . . . that is compatible with accepted definitions, yet allows nonintegrable spectra” (Reference 10). His succinct statement of the problem clearly implies that standard spectral theories, however useful, do not address the nonintegrable case. Fortunately, his new results include fBm with a spectrum obeying $f^{-\alpha}$ for $1 < \alpha \leq 2$, which is the interval of interest for staring focal plane arrays (FPAs). Fractional Brownian motion noise can model all of these different colored noises. The critical step in determining a model for the array noise is to estimate the parameter α , something that is hard to obtain from measured data. However, we do have a set of candidate statistics that we will use to estimate α . It should be noted that Scribner and others do not postulate a fractional Brownian motion model (Reference 1). However, they do report a mean pixel value for α of 1.2 for a midwave infrared FPA.

Published reports clearly recapitulate the existence of some type of $1/f$ noise in FPAs, and recent important theoretical progress clarifies the link between fractional Brownian motion, wavelets, and periodograms. If a strong case can be made for fBm as a reasonable model for staring array spatial noise, then a paradigm for point target detection in fBm can be formulated. In fact, recent studies by Wornell (References 11 and 12) and Barton and Poor (Reference 13) address the problem of signal detection in fractional Brownian noise. Their approach is similar to that already used with respect to radar, in which a target-

detection-strategy paradigm is defined by a maximum likelihood algorithm. The algorithm defines an optimum target-detection strategy with a false-alarm rate that must discriminate between fluctuating targets embedded in white noise and random clutter. Although such methods are not perfect, they are useful for design and do define detection algorithms. Thus, a determination of the array noise is an important basic step in establishing a similar detection agenda in staring FPAs. Another outgrowth of having a model for array noise is that novel array nonuniformity-compensation algorithms that incorporate fBm might be developed. Nonuniformity-compensation algorithms are necessary to correct for pixel nonuniformities, but $1/f$ noise and system instabilities foil many algorithms; thus, continuing recalibration is required.

In the next section of this report, FBm, Wavelets, and ARIMA Models, some important properties of fBm and wavelet transforms are reviewed. A key parameter in fBm is then identified with the exponent α in the $1/f$ -type spectra. Some concepts and operations from stochastic theory that are relevant to the definition of fBm are defined. Next, some statistical algorithms are introduced that can be used to directly measure the parameters in fBm. Autoregressive moving average models with fractional differencing first introduced by Hosking (Reference 14) are reviewed. Hosking's model provides simple and fundamental insight about the kind of discrete stochastic processes that obey $f^{-\alpha}$ behavior in a neighborhood of the origin. This discussion explains why fractional differencing and fractional sums are fundamental operations that are necessary to properly model fBm.

In the FBm Simulation and Examples section of this report, concepts and statistics introduced in the FBm, Wavelets, and ARIMA section are illustrated by using a Hosking algorithm to synthesize fBm. After the algorithm is introduced, sample paths and increments of fBm are presented along with their periodograms, autocorrelations, wavelet transforms, and marginal distributions. Some small sample studies of the statistics that have been proposed to estimate the fBm parameters are also presented.

Some details about the Amber camera experimental test conditions, some processed examples, and some measured parameters from the test are presented in the Amber Camera Test Results section. Some time samples from selected individual pixels and their increments are presented in a multipanel format along with their periodograms, autocorrelations, wavelet transforms, and marginal distributions. Thus, the analysis in this section is exclusively concerned with spatial noise. After the multipanel graphs, a table of key fBm parameters is presented that summarizes the results of 60 selected pixels that are sampled across the array.

FBm, WAVELETS, AND ARIMA MODELS

A flicker noise (FN) or 1/f-type process is a time series with a low-frequency spectrum $F(\omega)$ of the form $\omega^{-\alpha}$ $\alpha > 0$ in a neighborhood of the origin. When $\alpha \equiv 1$ then the time series exhibits a long-term temporal dependency. The study of such processes is somewhat paradoxical, because for $\alpha = 1$ the spectrum is not integrable on the semi-infinite interval $(0, \infty)$. This suggests that the model implies infinite variance and therefore that the spectrum of the process apparently cannot exist. Recently, Solo has shown that fractional Brownian motion is a mathematical model for FN that has a mathematically correct nonintegrable spectrum of the form $\omega^{-\alpha}$ with $1 \leq \alpha \leq 2$ (Reference 10).

Fractional Brownian motion is an example of a stochastic process. Stochastic process theory belongs to the "dynamic" part of probability theory and provides a mathematical theory of random events that occur in time or space. Stochastic processes include models for the random behavior of stock-market indexes, for the path of a particle in Brownian motion, for the number of particles emitted by a radioactive source, for ocean clutter fields, and for the behavior of queues, to name a few common examples. In this report the fractional Brownian model is proposed as a stochastic process that models the detector noise field present on infrared staring FPAs. Moreover, if one subscribes to the theory that 1/f noise is the ubiquitous spectrum for detector and semiconductor noise, then fBm may be expected to be a relevant model for many other devices.

Because the mathematical details are complex and are available to the interested reader in References 15 and 16, only the highlights of the necessary stochastic concepts are presented here. In general a stochastic process is a function $X(\cdot, \cdot)$ of at least two variables. One variable describes the observation point t , and the other variable represents the random event space Ω . The space of random variables Ω describes a set of random events that coincide with the observation point. Generally the dependency of the stochastic process $X(\cdot, \cdot)$ on the space of random variables Ω is suppressed, and only the dependency on the time variable is explicit. The observed time series $X(t)$ represents a "realization" or "sample path" of the stochastic process $X(\cdot, \cdot)$; thus, the value $X(t)$ at each time value is a random variable that depends on Ω . Generally the dependency on Ω is suppressed.

The average or expected value operation is of course useful in describing the properties of the stochastic process $X(t)$. Some of the common operations are denoted as follows:

mean $E(X(t))$, autocovariance $C_{XX}(t) = E(X^*(t)X(t)) - E(X(t))E(X(t))$, where $*$ denotes complex conjugate and autocorrelation function $C_{XX}(t) / \sqrt{C_{XX}(t)^* C_{XX}(t)}$

Given a set of discrete samples of a stochastic process, the autocorrelation becomes the sum for $M \leq N$ (Reference 17):

$$c_{xx}(m) = \frac{1}{N} \sum_{n=0}^{N-|m|-1} x(n)x(n+m), \quad 0 \leq m \leq M-1$$

If the sample mean is first subtracted from $x(n)$, then $c_{xx}(m)$ is an estimate of the autocovariance, and the autocovariance divided by the square root of $c_{xx}(0)$ (standard deviation) is the correlation. Sometimes the term "auto" is omitted when the operational variables are unambiguous.

The concept of stationary for a time series is analogous to the concept of steady-state analysis for time-invariant systems. Roughly speaking, a stochastic process is called stationary if some major property is invariant with respect to a time translation of the time axis. A stochastic process defined on some space Ω and over some time interval T is stationary if the statistics are not affected by a shift in the time origin. This means that the statistics of $X(t)$ and $X(t + \tau)$ are the same for all $\tau \geq 0$.

A stochastic process defined on some space Ω and over some time interval T is weakly stationary or covariance stationary if the mean and variance are the same for all time and if its covariance $\text{cov}(X(t), X(s))$ depends only on the absolute difference $|s - t|$ for every s and t in T .

If a process is stationary then it is weakly stationary; however, the converse is not true, because covariance stationary involves only the first two moments. A stochastic process $X(t)$ defined on some space Ω and over some time interval T has stationary increments if the probability properties of the process

$$\nabla X(t) = X(t) - X(t - \tau)$$

depends only on the lag variable τ .

Mandelbrot and Van Ness (Reference 18) introduced the class of stochastic processes called fractional Brownian motion (fBm), which includes ordinary Brownian motion as a special case. The process is denoted as $B_H(t)$ and is a zero-mean nonstationary stochastic

process that is indexed by a single scale parameter H . Here we assume that $B_H(0) = 0$ for convenience. The fBm covariance has the following form for $0 < H < 1$:

$$\text{cov}(B_H(t, s)) \equiv E[B_H(t)B_H(s)] = \frac{\sigma^2}{2} (|s|^{2H} + |t|^{2H} - |t-s|^{2H})$$

When the index $H = 1/2$, the fBm is ordinary Brownian motion. With the covariance equation, the following inequalities for the covariance equation can be deduced for $t > 0$ and $0 < H < 1$ using the simple chain of inequalities (for $H < 1/2$ a similar chain can be deduced).

$$2 \geq 2^{2H} \Leftrightarrow \log_2 2 \geq 2H \log_2 2 \Leftrightarrow \frac{1}{2} \geq H$$

$$\text{COV}(B_H(t)B_H(-t)) = E[-B_H(t)B_H(-t)] = \begin{cases} > 0 & \text{if } H > \frac{1}{2} \\ = 0 & \text{if } H = \frac{1}{2} \\ < 0 & \text{if } H < \frac{1}{2} \end{cases}$$

When for $H = 1/2$ the past and future increments are not correlated, otherwise fBm exhibits persistence or antipersistence as a function of the index H . For $H > 1/2$ persistence rules, which means past increasing or decreasing trends are on the average replicated in the future. Antipersistence occurs when $H < 1/2$; in this case past increasing or decreasing trends are anticyclical in the future. Persistence is the presence of significant dependence between observations that are a long span apart, whereas a common model for time series is that observations separated by a long time span are nearly independent. For this reason fBm is useful for modeling the time series of phenomena that exhibit persistence over a wide range of time scales. These concepts and an exact expression for the covariance are found in Reference 19.

It follows from the covariance equation that the variance of fBm satisfies

$$\text{var}(B_H(t)) \equiv E[B_H(t)B_H(t)] = \sigma^2 |t|^{2H}$$

and diverges with increasing time.

Although fBm is not weakly stationary, $\nabla B_H(t)$ has stationary increments. Moreover, this increment process is self-similar for any $a > 0$ where equality means equality in distribution (i.e., the statistics of fBm are invariant to time scaling).

$$B_H(at) = a^H B_H(t)$$

This self-similarity means that a realization of such a process is a fractal curve, and its fractal dimension D is $D = 2 - H$ (Reference 20).

A specialized definition of fBm $X_B(t)$ is given by the expression found in Ramanathan and Zxeitouni (Reference 21). For the index H $0 < H < 1$ and the zero-mean, stationary white Gaussian noise random process $w(t)$ with unit spectral density, the density is

$$X_B(t) \equiv \frac{1}{\Gamma(H+.5)} \left[\int_{-\infty}^0 (|t-\tau|^{H-1/2} - |\tau|^{H-1/2}) w(\tau) d\tau + \int_0^{\infty} |t-\tau|^{H-1/2} w(\tau) d\tau \right]$$

where Γ represents the Gamma function. The proper mathematical definition of the spectrum of fBm is a delicate matter. To justify fBm as a model for $1/f$ -type processes or FN means that at low frequencies its spectrum approximates $\omega^{-\alpha}$. Recently, some important new results by Flandrin (References 22 and 23), Hosking (Reference 14), Solo (Reference 10), and Wornell (References 11 and 12) have all made significant progress in refining the mathematical connections between fBm and its $1/f$ -type spectrum. Hosking shows that a family of autoregressive integrated moving average (ARIMA) processes with fractional differencing has a $\omega^{-\beta}$ spectrum. Flandrin uses a wavelet transform to show how the spectrum of fBm can be estimated and defined, and Wornell uses a wavelet transform to produce models that approximate a $1/f$ -type spectrum. Solo justifies the estimation of α in fBm spectra $\omega^{-\alpha}$ from n discrete time data samples by the slope of a log-log plot. The plot is the log of the periodogram versus the log of ω . The periodogram is the squared modulus of the discrete Fourier transform of the data.

To demonstrate that the spectrum of fBm behaves as $\omega^{-\alpha}$, Flandrin starts with the wavelet of fBm, which is defined as

$$W(b, a) \equiv \frac{1}{\sqrt{a}} \int_{-\infty}^{\infty} B_H(t) g\left(\frac{t-b}{a}\right) dt$$

Here g is any wavelet with scale parameter a whose Fourier transform \mathfrak{F} satisfies the admissible condition

$$\int_{-\infty}^{\infty} \frac{|\mathfrak{F}(g(\omega))|^2}{|\omega|} d\omega < \infty \quad (1)$$

where $\mathfrak{F}(g(\omega))$ is the Fourier transform of $g(t)$. If $\mathfrak{F}(g(\omega))$ is differentiable, then it suffices that g be zero mean, i.e., $\int_{-\infty}^{\infty} g(t) dt = 0$, for Equation 2 to be satisfied (References 24 through 26).

As shown by Flandrin, the covariance of $W(b,a)$ is a function only of $\frac{t-s}{a}$ and thus $W(t,a)$ is a weakly stationary stochastic process. In other words, when the nonstationary process $B_H(t)$ is analyzed at a fixed scale, it is weakly stationary! Thus, the Fourier transform of $\text{cov}(W(t,a)W(s,a))$ is well defined. So taking the average of the Fourier transform \mathfrak{F} of $\text{cov}(W(t,a)W(t,a))$ and integrating over all scales using the normalizing measure yields

$$\int_0^{\infty} \mathfrak{F}(\text{cov}(W(t,a)W(t,a))) \frac{da}{a^2} = \frac{1}{\omega^{2H+1}} \quad (2)$$

Thus, Flandrin has established a direct connection between the wavelet approach and the $1/f$ -type process. Another remarkable result about the wavelet transform and fractional Brownian motion has been established by Flandrin. To explain his result some additional facts about wavelet transforms are now introduced.

Wavelets are not arbitrary functions, and as a minimum they satisfy the Fourier condition defined by Equation 1. The wavelets $\psi(t)$ introduced by Daubechies (Reference 24) are obtained from the scaling function $\phi(t)$, which is the solution of the two scale difference equation (a dilation equation):

$$\phi(t) = \sum_k c_k \phi(2t - k)$$

If the coefficient sequence $\{c_k\}$ is finite in length, the wavelet $\psi(t)$ has compact support. The sequence $\{c_k\}$ satisfies the following conditions, which are respectively a normalizing condition, an orthogonality condition (δ_{mn} is the discrete Dirac delta function), and a regularity or vanishing moment condition.

$$\sum c_k = \sqrt{2}, \quad \sum c_k c_{k-2m} = 2\delta_{0m}, \quad \sum (-1)^k k^m c_k = 0, \quad m = 0, 1, \dots, p-1$$

The wavelet equation is constructed from the sequence $\{c_k\}$ by the quadrature mirror condition

$$\psi(t) = \sum_k (-1)^k c_{1-k} \phi(2t-1)$$

The Haar wavelet has compact support is quite simple and is defined as follows:

$$\psi(t) = \begin{cases} +1 & 0 \leq t < 1/2 \\ -1 & 1/2 \leq t < 1 \\ 0 & \text{otherwise} \end{cases}$$

The scaling function is

$$\phi(t) = \begin{cases} +1 & 0 \leq t < 1 \\ 0 & \text{otherwise} \end{cases}$$

Although Haar wavelets are simple and compact in the time domain, they are not well localized in Fourier space where they decay very slowly as ω^{-1} . Wavelets that are well localized in both time and Fourier space have been discovered only recently by Daubechies (Reference 24). Wavelets that decay as rapidly as ω^{-4} in Fourier space and exponentially in the time domain are discussed by Mallat (Reference 27). Wavelets that are well localized in both time and space provide a reasonably sharp decomposition of the signal in both domains. The localization is limited to bands of nonzero thickness in both t and ω space because of the Fourier or Heisenberg uncertainty principle.

The Hilbert space of measurable square integrable functions is denoted by $L^2(R)$, i.e., the space of signals $f(t)$ with finite energy, satisfying

$$\int_{-\infty}^{\infty} |f(t)|^2 dt < \infty$$

The compactly supported Daubechies wavelet forms an orthonormal basis for $L^2(R)$, which means that any function that is a member of $L^2(R)$ can be expanded into a wavelet series instead of a Fourier series. A function that is a member of $L^2(R)$ has "finite power" and can be expanded into a series using the sequence of wavelets $\{\sqrt{2^j} \psi(2^j t - m)\}$ as the

basis functions. Moreover, for some wavelets all translates and dilates of $\psi(t)$ are mutually orthogonal using the inner product $\langle * \rangle$.

$$\langle \sqrt{2^k} \psi(2^k t - l), \sqrt{2^j} \psi(2^j t - m) \rangle = \delta_{jk} \delta_{ml}$$

The discrete wavelet coefficients that represent the expansion in the scaling functions are called the approximation coefficients $a_j(n)$

$$a_j(n) = \langle f(t), \sqrt{2^j} \phi(2^j t - n) \rangle = \sqrt{2^j} \int_{-\infty}^{\infty} f(t) \phi(2^j t - n) dt$$

where $f(t)$ is any function in $L^2(R)$. The wavelet expansion coefficients are called the detail coefficients $d_j(n)$, because they represent the difference between two successive approximations and are computed as follows (Reference 25).

$$d_j(n) = \langle f(t), \sqrt{2^j} \psi(2^j t - n) \rangle = \sqrt{2^j} \int_{-\infty}^{\infty} f(t) \psi(2^j t - n) dt$$

For any finite integer J , $\{\sqrt{2^J} \psi(2^J t - m) \cup \sqrt{2^J} \phi(2^J t - m)\}$ is an orthonormal basis for $L^2(R)$. Thus, any function $f(t)$ in $L^2(R)$ can be written as the infinite series

$$f(t) = \sqrt{2^J} \sum_{m=-\infty}^{m=\infty} a(m) \phi(2^J t - m) + \sum_{j=J}^{\infty} \sum_{m=-\infty}^{m=\infty} \sqrt{2^j} d_j(m) \psi(2^j t - m)$$

This series expansion is called a multiresolution decomposition of $f(t)$. The decomposition is multiresolution, because the approximation coefficients and the detail coefficients are computed at successively different scales indexed by j . Note the different role played by the approximation coefficients and the detail coefficients in the expansion. Of course, for any discrete sequence $\{x_0, \dots, x_{n-1}\}$ the discrete wavelet transform is actually computed. A detailed and insightful discussion of the discrete wavelet transform is found in the report by Shensa (Reference 28).

The diagram in Figure 1 illustrates the standard orthonormal fast wavelet transform. The solid vertical line represents the division between the analysis (decomposition) and synthesis (reconstruction) parts of the transform. The input vector x represents a discrete data sequence that is convolved on the parallel branches via the two discrete filters g and h . The coefficients for the two filters are obtained from the wavelet and scaling function,

respectively. The arrow $\downarrow 2$ means drop every second sample. The 2 is the dilation factor for use with wavelets with one octave bandwidth. The output from the top branch represents the detail coefficients $d_j(n)$, and the output from the bottom branch represents the approximation coefficients $a_j(n)$. If the wavelet transform uses orthogonal wavelets, then either or both sets of output coefficients may be used as the new input vector x . When both $d_j(n)$ and $a_j(n)$ are used as separate and parallel inputs for the analysis stage, then a wavelet packet hierarchical or tree-structured signal decomposition is produced. The synthesis is also hierarchical in nature and reconstructs a final signal \hat{x} by using the detail coefficients $d_j(n)$ on the top branch and the approximation coefficients $a_j(n)$ on the bottom branch. The $\uparrow 2$ arrow means insert one zero between samples. Generally the filters \hat{g} and \hat{h} are related to g and h , but as long as they represent a valid orthogonal wavelet scaling function pair the synthesis branch can use a different wavelet. The diagram in Figure 1 represents a fast dyadic (or two-band) wavelet transform for doing multiresolution processing as introduced by Mallat (Reference 28) and Daubechies (Reference 24). Recently, Zou and Tewfik (Reference 29) have constructed M-band generalizations that have a similar block diagram with multiple parallel branches for the additional M-1 wavelet filters, and the $\downarrow 2$ block is replaced with \downarrow . M. Cohen and Daubechies (Reference 30) have shown how to construct rational band orthogonal wavelet bases with 1/2-octave or even smaller bandwidth wavelets.

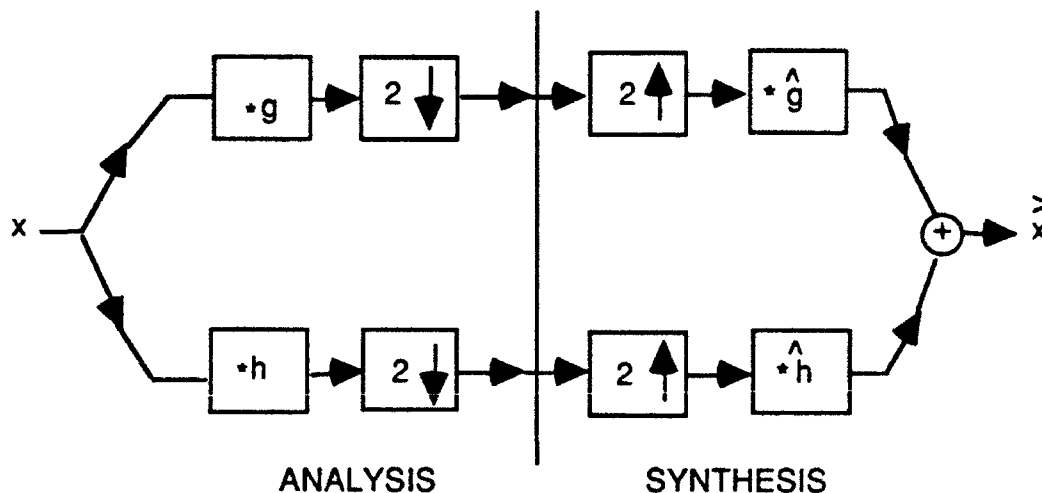


FIGURE 1. Fast Wavelet Transform Block Diagram.

Flandrin has shown that the detail coefficients have stationary properties after a wavelet transform is applied to fBm (Reference 23)! Tewfik and Kim have shown that the vanishing moment property of the Daubechies wavelets controls the correlation at a given scale and between scales (Reference 31). In integral terms the wavelet $\psi(t)$ has M vanishing moments if

$$\int_{-\infty}^{\infty} t^m \psi(t) dt = 0 \quad m = 0, 1, \dots, M-1 \quad \text{for } M > 0$$

Not all wavelets have compact support, nor are they all orthonormal functions. In fact, Mallat and Zhong have shown that multiresolution edge detection wavelets are not orthogonal (Reference 32). All of these topics and formulas for many other interesting wavelets can be found in the excellent monograph by Daubechies (Reference 25).

Hosking models $1/f$ -type processes by starting with an ARIMA(0,d,0) process with $|d| < \frac{1}{2}$ for the ω^{2d} spectrum and then extending it to a ARIMA(p,d,q) process (Reference 33). When d is an integer, then ARIMA(p,d,q) denotes the usual ARIMA process with p coefficients for the autoregressive process, d^{th} integral differences, and q coefficients for the moving average process. To summarize the important properties of the ARIMA(0,d,0) process model for fBm, let us define the differencing operator ∇ , which, when applied to a discrete sequence (discrete time signal) $x(n)$, yields the derived sequence

$$\nabla x(n) = (1 - B)x(n) = x(n) - x(n-1)$$

where B is the backward shift operator $Bx(n) = x(n-1)$. Fractional differencing is obtained by repeated applications of B d times, where d is a real number. The operation is formally defined by the binomial expansion of the operator ∇^d :

$$\begin{aligned} \nabla^d x(n) &\equiv (1 - B)^d x(n) = \sum_{k=0}^{\infty} \binom{d}{k} (-B)^k x(n) \\ &= x(n) - dx(n-1) - \frac{1}{2} d(1-d)x(n-2) - \frac{1}{6} d(1-d)(2-d)x(n-3) - \dots \end{aligned} \quad (3)$$

For $|d| < \frac{1}{2}$ the infinite series converges in mean square and so the operation ∇^d is well defined. The ARIMA(0,d,0) is the discrete time sequence $x(n)$ that is represented by the following equation:

$$\nabla^d x(n) = e(n)$$

where the operator ∇^d is defined in Equation 3 and the white-noise Gaussian input $e(n)$ is a sequence of independent and identically distributed random zero-mean variables satisfying the equations

$$E(e(n)) = 0$$

$$E(e(n)e(j)) = \begin{cases} \sigma^2 & \text{for } n=j \\ 0 & \text{for } n \neq j \end{cases}$$

The Hosking ARIMA(0,d,0) model is discrete fractional Gaussian noise (fGn). Discrete fBm is then generated by adding up the increments. The ARIMA(0, $\frac{1}{2}$, 0) process is fGn with a 1/f spectrum, while the ARIMA(0,0,0) process is fGn with constant spectral density. It has some very interesting properties that qualify it as a candidate for fBm. If $x(n)$ is an ARIMA(0,d,0) process for $|d| \leq \frac{1}{2}$, then $x(n)$ is stationary with 1/f-type spectral density:

$$S(\omega) \equiv \text{spectrum}(\omega) = (2 \sin \frac{1}{2} \omega)^{-2d} \quad 0 < \omega \leq \pi \quad S(\omega) \approx \omega^{-2d} \quad \text{as } \omega \rightarrow 0$$

The correlation function of $x(n)$ is as $k \rightarrow \infty$

$$\rho^k = \frac{d(1+d) \cdots (k-1+d)}{(1-d)(2-d) \cdots (k-d)} \approx \frac{\Gamma(1-d)}{\Gamma(d)} k^{2d-1} \quad (4)$$

where Γ represents the Gamma function. The partial correlations of $x(n)$ are

$$\phi_{kk} = d/(k-d) \quad k = 1, 2, 3, \dots$$

For the $d \leq 0$ ARIMA(0,d,0) process, the correlation decays hyperbolically as the lag increases, as opposed to exponential decay of short-term memory processes that are typical of autoregressive moving average (ARMA) (p,q) processes, which are now defined.

In the digital signal processing literature, ARMA processes are simply time-invariant constant coefficient difference equations. An autoregressive process (AR(p)) is a linear difference equation with constant coefficients driven by white noise. The autoregressive process is defined as a real random sequence $X(n)$ with real coefficients $\psi_{p,i}$ and input $e(n)$:

$$X(n) = \sum_{i=1}^p \psi_{p,i} X(n-i) + e(n) \quad \psi_{p,p} \neq 0$$

The AR(1) model is the first-order difference equation

$$X(n) = \psi_{1,1}X(n-1) + e(n)$$

which is stationary and has a finite variance when $|\psi_{1,1}| < 1$. Moreover, the difference equation is stable and has an autocorrelation function that decays exponentially:

$$\rho^m = \frac{c_{XX}(m)}{c_{XX}(0)} = \psi_{1,1}^m$$

A comparison of the two autocorrelation functions for the AR(1) and the ARIMA(0,d,0) processes clearly reveals the difference between persistence and short memory processes. The autocorrelation coefficients for the AR(1) decay exponentially and are positive or oscillate in sign as $m \rightarrow \infty$, whereas the coefficients in Equation 4 for the ARIMA(0,d,0) process decay hyperbolically as $k \rightarrow \infty$.

A moving average process (MA(q)) is a linear difference equation with constant coefficients driven by white noise. It is defined as a real random sequence $X(n)$ with real coefficients $\vartheta_{q,i}$ and white-noise input $e(n)$:

$$X(n) = \sum_{i=1}^q \vartheta_{q,i}e(n-i) + e(n) \quad \text{where } \vartheta_{q,q} \neq 0$$

The ARIMA(0,d,0) process has three free parameters: the fractional difference d , the mean, and the variance of the process. The ARIMA(p,0,q) processes have the $p + q$ coefficients as free parameters. Thus, the Hosking ARIMA(p,d,q) process, with p coefficients for the autoregressive process, fractional differences d , and q coefficients for the moving average process, is a combination of the above models. The model has the ARIMA(p,0,q) process to account for the short-term properties and the ARIMA(0,d,0) process to account for the long-term persistent behavior of the observed time series. An algorithm for simulating both the ARIMA(p,d,q) and ARIMA(0,d,0) processes is defined by Hosking (Reference 33) and is used in this report to model these processes.

The ARIMA(p,d,q) processes satisfy the following equation with mean μ and fractional difference operator ∇^d of order d . In this equation, $e(n)$ is the white-noise sequence defined for the ARIMA(0,d,0) process polynomial operators defined for the operator B .

$$\begin{aligned} \phi(B)\nabla^d(y(n) - \mu) &= \vartheta(B)e(n) \\ \phi(B) &\equiv 1 - \phi_1 B - \dots - \phi_p B^p \\ \vartheta(B) &\equiv 1 - \vartheta_1 B - \dots - \vartheta_q B^q \end{aligned}$$

In order to explain the connection between the range of the parameter H in Equation 2 and the d in the fGn ARIMA(0,d,0) model, we need to know the relationship between the spectrum $S_{x(n)}(\omega)$ of the image sequence x(n) and the spectrum $S_{y(n)}(\omega)$ of the image sequence y(n)

$$y(n) = \nabla^d x(n)$$

that is obtained by applying the fractional differencing operator ∇^d to x(n) d times. Based on filtering considerations (Reference 34), the relationship between the two spectrums can be formally written as

$$S_{y(n)}(\omega) = |1-z|^{-2d} \nabla^d x(n)(\omega) \quad \omega \neq 0$$

where $z = e^{-i\omega}$. This transfer function relationship follows when we note that the z-transform for $(1 - \nabla)$ is $1 - z$. When the sequence is differenced once (i.e., $d=1$), the spectrum is multiplied by $|1-z|^2 = 2(1 - \cos \omega)$. Next we note that $(1 - \cos \omega) = 2(\sin \frac{\omega}{2})^2$, and we have in a neighborhood of the origin

$$S_{y(n)}(\omega) = \left(\frac{1}{\omega^2}\right) S_{\nabla^1 x(n)}(\omega) \quad \omega \neq 0$$

The equation $H = d + \frac{1}{2}$ combined with Equation 5 implies that the fGn ARIMA(0,d,0) model with power spectrum of the form $\frac{1}{\omega^{2+d}}$ in a neighborhood of the origin produces a power spectrum for the fBm x(n) of the form $\frac{1}{\omega^{2H+1}}$. Thus, d in the interval $0 \leq d < \frac{1}{2}$ yields $\frac{1}{2} \leq H < 1$, while the interval $-\frac{1}{2} \leq d < 0$ yields $0 < H \leq \frac{1}{2}$. This relationship implies that in the Brownian increment process with persistent behavior, as discussed in Reference 19, $0 < d < \frac{1}{2}$ produces a spectrum for the fBm sample path of the form ω^{-2H-1} in a neighborhood of the origin $2 < 2H + 1 < 3$, while antipersistent behavior $-\frac{1}{2} < d < 0$ yields $1 < 2H + 1 < 2$. Thus, the Hosking model provides a general approach to the discrete 1/f-type processes with a simple and logical relation between the parameters. For antipersistent behavior, Solo develops the connection between FN and fBm by providing a firm theoretical foundation for the proper interpretation of the power spectrum (Reference 10). A paper by Haslett and Raftery (Reference 35) is a comprehensive study of time series with persistent behavior.

One of the fascinating historical aspects of fBm is the Hurst rescaled range statistic. In fact, it is the reason that Mandelbrot used H for the exponent in the power spectrum of the sample path of $B_H(t)$ (Reference 20). The Hurst coefficient and the d in Hosking's ARIMA(0,d,0) process are related by the equation $H = d + 1/2$. However, the power spectrum $\frac{1}{\omega^{2d}}$ for the fGn ARIMA(0,d,0) process applies to the increments $\nabla B_H(t) = B_H(t) - B_H(t-1)$. The distinction between estimates that is applied to the sample path of a time series (e.g., $B_H(t)$) or to the increments of the time series (e.g., $\nabla B_H(t)$) is important, and one must be alert to these alternatives when consulting the literature in this field.

To compute the Hurst coefficient, a statistic for the range R of a discrete data sequence is defined. An explicit expression for R is

$$R(\tau) = \max_{1 \leq t \leq \tau} X(t, \tau) - \min_{1 \leq t \leq \tau} X(t, \tau)$$

where t is a sampled value of the time series $X(t)$ and τ is the time span considered. To devise a statistic that could discriminate between long- and short-term time scales, Hurst uses the dimensionless ratio R/S where S is the estimated standard deviation defined as follows for the time series $x(t)$:

$$\langle x \rangle_\tau = \frac{1}{\tau} \sum_{t=1}^{\tau} x(t), \quad S = \left(\frac{1}{\tau} \sum_{t=1}^{\tau} \{x(t) - \langle x \rangle_\tau\}^2 \right)^{\frac{1}{2}}$$

Finally the coefficient H is found using a log-log plot from the empirical relation:

$$\frac{R}{S} = \left(\frac{\tau}{2} \right)^H$$

Schroeder reports that the Hurst coefficient for the Nile river level minima taken between the years 622 B.C. and 1469 B.C. has $H = 0.9$, or a spectrum of $\omega^{-2.8}$ (Reference 9). The equation $H = d + 0.5$ yields $d = 0.4$ for the corresponding Hosking ARIMA(0,d,0) process. The Hurst coefficient thus quantifies the legendary cycles of the Nile's annual floods.

FBm SIMULATION AND EXAMPLES

In this section the ARIMA(0,d,0) algorithm of Hosking is used to simulate fBm with spectrum $\frac{1}{\omega^{2H+1}}$ and fGn with spectrum $\frac{1}{\omega^{2d}}$. A number of different statistics for estimating the parameters of fBm are illustrated. These statistics include the Hurst coefficient, the wavelet transform, the periodogram, and some new iterative algorithms by Deriche and Tewfik (Reference 36). The new iterative algorithms are used to estimate the parameters in the ARIMA(0,d,0) models. Throughout this section the distinction between the sample path $B_H(t)$ of fBm and the increments $\nabla B_H(t)$ will be observed.

An algorithm to simulate ARIMA(p,d,q) models (p and q non-negative integers, $|d| < \frac{1}{2}$) is derived by Hosking (Reference 14). When p = q = 0, the algorithm simulates the sample increments $\{x_0, \dots, x_{n-1}\}$ of $\nabla B_H(t)$ of size n with a normal marginal distribution and correlation function ρ_k . The sample path $B_H(t)$ is the sum over $\nabla B_H(t)$. For completeness the algorithm for the general ARIMA(0,d,0) model is reproduced here and defined as follows:

1. Generate the starting value x_0 from a normal or Gaussian distribution $N(0, \sigma_0)$ with mean zero and variance σ_0 ($\sigma_0 = \text{var}(\{x_0, \dots, x_{n-1}\})$).

2. For t=1, ..., n-1, define the recursive equations for ϕ_{ij} j=1, ..., t

$$\phi_{it} = d/t - d$$

$$\phi_{ij} = \phi_{i-1,j} - \phi_{it} \phi_{i-1,t-j} \quad j = 1, \dots, t-1$$

Calculate $m_t = \sum_{j=1}^t \phi_{ij} x_{t-j}$ and $v_t = (1 - \phi_{it}^2) v_{t-1}$. Generate the next x_t from $N(m_t, v_t)$.

The multipanel graphics in this report were generated using *S-PLUS*^{®1}, which was also a valuable source for many of the basic statistical algorithms utilized in the preparation of this report.

¹ *S-PLUS*[®] is a registered trademark of Statistical Sciences, Inc., Seattle, Washington.

All of the sample paths $B_H(t)$ or realizations plotted in Figures 2 and 3 for fBm start with $n = 3,000$ sample increments $\{x_0, \dots, x_{n-1}\}$ for $\nabla B_H(t)$. The sample paths $B_H(t)$ or realizations are generated by the Hosking ARIMA(0,d,0) model (Reference 33). In Figure 2 three examples of simulated fBm are illustrated. The sample paths are illustrated in panels a, c, and e with corresponding d values of 0.4, 0, and -0.4. Each fBm realization has a Gaussian marginal distribution with zero mean and unit variance. In Figure 14 the Gaussian shape of the marginal distributions will be examined by the use of quantile-quantile (Q-Q) plots (Reference 37), and in Figure 15 the shape of the marginal distributions will be estimated by histograms and by empirical density approximation. Panels b, d, and f are the corresponding periodograms, which are log-log plots of the periodogram $X(\omega)$ versus the log of the frequency variable ω . The periodogram $X(\omega)$ is the modulus of the Fourier transform $\mathfrak{F}(x(n))$ of the discrete sequence $\{x_0, \dots, x_{N-1}\}$

$$X(\omega) = \left(\frac{1}{N}\right) \mathfrak{F}(x(n)) \mathfrak{F}(x(n))^*$$

where N is the total number of samples and $()^*$ is the complex conjugate. The index H can be estimated from the slope of the dotted line. It is the least squares fit to the lower frequencies on the log-log plot of the periodogram.

Tables 1 and 2 compare the performance of all of the statistics that have been defined in this report. These include the log-log plots whose slopes are used to estimate \hat{H} . The one new estimate for \hat{H} is by Raftery (Reference 35) and it is obtained by using his Fortran program called `fracdiff`².

These tabulated results are based on a limited sample and are meant to suggest only the comparative variability among the different statistics. All of the statistics in the first four rows of Table 1 are based on samples that used the same value of d , namely, $d = 0.4$ or equivalently $H = 0.9$. The statistics in the last row of Table 1 are based on samples that used $d = -0.4$ or equivalently $H = 0.1$. The column headings Hurst, Wavelet, Spectrum, and Variance are defined by matching them with Table 2. All of the former statistics are based on sample paths B_H , and `fracdiff`, which estimates \hat{d} is based on the increments ∇B_H . The Daubechies wavelet D_{10} was used exclusively in the wavelet estimates. When two estimates are given in the table, it is because the statistics are based on linear fits obtained by the *S-PLUS* routines least squares fit (`lsm`) and least median squares regression (`lms`).

² `fracdiff` is a function in StatLib obtainable via an anonymous FTP.

TABLE 1. Comparative Statistics for the Estimation of the Index H.

| No. of samples | fracdiff \hat{d} (d=0.4) | Hurst \hat{H} (H=0.9) | Wavelet \hat{H} (H=0.9) | Spectrum \hat{H} (H=0.9) | Variance \hat{H} (H=0.9) |
|----------------|-------------------------------|----------------------------|------------------------------|-------------------------------|-------------------------------|
| 1000 | 0.412429 | 0.81981 | 0.850106(ls) 0.86927(lm) | 0.897877 | 0.6638(ls) 0.7184(lm) |
| 2000 | 0.422846 | 0.8529 | 0.849(ls) 0.939(lm) | 0.9078(ls) | 0.7723(ls) 0.7881(lm) |
| 3000 | 0.40855 | 0.82313 | 0.8354(ls) 0.8981(lm) | 0.83944 | 0.71232(ls) 0.79531(lm) |
| 5000 | 0.423665 | 0.92279 | 0.7964(ls) 0.8985(lm) | 0.84638 | 0.8550(ls) 0.8883(lm) |
| | | \hat{H} (H=0.1) | \hat{H} (H=0.1) | \hat{H} (H=0.1) | \hat{H} (H=0.1) |
| 5000 | --- | 0.2652(ls) 0.2749(lm) | 0.07068(ls) 0.07212(lm) | 0.0811(ls) 0.0794(lm) | 0.1347(ls) 0.1919(lm) |

As expected, the estimates for \hat{H} obtained by fracdiff are the most accurate, because the program is based on more comprehensive statistical theories. Unfortunately, the version used for this study could only be used estimate \hat{d} for the persistent case (i.e., $0 < d < 1/2$). None of the other statistics did an outstanding job. They all give rough estimates, however, after rounding to one significant figure. \hat{H} is bounded in the interval defined by the maximum and minimum among the three statistics, Hurst, wavelet, and spectrum.

Table 2 represents a small sample study of the effects of white noise on the various statistics. These are all estimated from the sample path of an ARIMA(0,d,0) model plus additive white Gaussian noise N(0,4).

Table 2 clearly demonstrates that the statistics are sensitive to the white noise; however, this is to be expected, because their robustness has not been assessed. Based on this small sample study, it appears that Spectrum is the most reliable estimator. This is partially based on the fact that an inspection of the periodogram can be made before a frequency band for the least squares fit is selected. The inspection procedure avoids the white-noise knee in the periodogram that is clearly evident by comparing Figures 2 and 13. Clearly, a more accurate estimator like fracdiff is needed. The method of Wornell (Reference 12), which uses the maximum likelihood algorithm, will undoubtedly provide better estimates for the

fBm parameters H and σ^2 and for the corrupting white-noise variance σ_w^2 than the statistics used in this exploratory study.

TABLE 2. Comparative Statistics for the Estimation of the Index H .

| No. of samples | Hurst \hat{H} ($H=0.9$) | Wavelet \hat{H} ($H=0.9$) | Spectrum \hat{H} ($H=0.9$) | Variance \hat{H} ($H=0.9$) |
|----------------|---|---|---|---|
| 3000 | 0.72244(l _s) 0.65170(l _m) | 0.6878534 | 0.92753(l _s) 0.77685(l _m) | 5925(l _s) 0.63523(l _m) |
| 5000 | 0.67198(l _s) 0.72429(l _m) \hat{H} ($H=0.1$) | 0.75177(l _s) 0.82517(l _m) \hat{H} ($H=0.1$) | 0.91378(l _s) 0.66926(l _m) \hat{H} ($H=0.1$) | 0.62605(l _s) 0.67901(l _m) \hat{H} ($H=0.1$) |
| 3000 | 0.13528(l _s) 0.194905(l _m) | 0.28619(l _s) 0.25856(l _m) | 0.03339(l _s) 0.03987(l _m) | 0.05932(l _s) 0.048578(l _m) |
| 5000 | 0.1745(l _m) 0.1730(l _s) | 0.55200(l _s) 0.7107(l _m) | 0.0967(l _s) 0.0568(l _m) | 0.04815(l _s) 0.5684(l _m) |

In Figure 3 the identical $B_H(t)$ realizations from Figure 2 are plotted in panels a, c, and e. Panels b, d, and f in Figure 3 are the corresponding correlation. Note how panels b, d, and f all clearly exhibit slow decay with hyperbolic shape and positive correlation coefficients that distinguish persistent ($d > 0$) and antipersistent ($d < 0$) long-term behavior. The mathematical details can be found in Reference 33 and in Equation 4. These correlations indicate a significant dependence between observations well separated in time. This behavior is in contrast with observations that are nearly independent over long time spans.

In Figure 4 panels b, d, and f are the corresponding correlations for the increments $\nabla B_H(t)$ that are plotted in panels a, c, and e. Even in the increments the hyperbolic shape of the correlation function is evident in panel b. As expected, a significant change in correlation has occurred for the fGn ARIMA(0,d,0) model for $d = 0$ and for $d = -0.4$, and it suggests a significant decorrelation.

Both Haar's and Daubechies' scaling functions and wavelets are plotted in Figure 5. Panels a, c, and e contain the scaling functions; the wavelets are shown in the other panels. Panels a and b are the Haar wavelets, and the other panels contain the Daubechies wavelets. They are denoted D_4 and D_{10} , and their values are tabulated in Daubechies' seminal paper (Reference 24). The subscripts denote the number of vanishing moments; two times it is

the minimal number of coefficients that are necessary to implement the respective Daubechies wavelets via the discrete wavelet transform. Incidentally, D_1 is the Haar wavelet.

Figures 6, 7, 8, and 9 illustrate the different values of the wavelet transform operating on the $B_H(t)$ realizations. The parameter d in the ARIMA(0,d,0) model equals 0.4 in Figures 6 and 8 and -0.4 in Figures 7 and 9. Panels b, d, and f in each of these figures are plots of the detail coefficients $d_j(n)$ $j = 1, 2, 3$ for the corresponding wavelet transform. In each figure panel c is the correlation evaluated using the third scale detail coefficients $d_3(n)$. Panel c in each of these figures indicates that the wavelet transform does very well in decorrelating or whitening the fBm process, but it is clearly dependent on the sign of the parameter d . The ability of wavelets to favorably transform the fBm is the basis for the filtering theory presented by Chou (Reference 38). The reason for this fortuitous transformation is given by Flandrin (Reference 23) and Tewfik and Kim (Reference 31).

The decay of the correlation coefficients is directly controlled by the vanishing moment properties of the wavelet:

$$\int_{-\infty}^{\infty} t^m \psi(t) dt = 0 \quad m = 0, 1, \dots, M-1 \quad \text{for } M > 0$$

Panel e in each figure is a plot of the approximation coefficients $a_j(n)$ at the scale $j = 3$. The number of vanishing moments for D_4 and D_{10} are 4 and 10.

As a proposed model for the detector noise on staring arrays, fBm has three parameters (the mean μ , the variance σ , and the Hurst coefficient H) that must be estimated directly from measurements. Of the three parameters, the index H is the most difficult to estimate and is clearly the most important. In Figures 10 and 11 the index or Hurst coefficient \hat{H} is estimated using the rescaled range and the wavelet transform. In panels a, c, and e, \hat{H} is estimated from the slope on the log-log plot. In all panels a, c, and e, the solid line connects the values of the variance at the respective scales ranging from 1 to 6 or 7, and the dotted lines are the least squares fit. The vertical axis is the variance computed from wavelet detail coefficients and the horizontal axis is the scale. The estimate depends on the equation presented by Mallat (Reference 27).

$$\log_2(\text{var}(d_j(n))) = (2H)j + \text{constant}$$

This procedure is derived by Flandrin (Reference 22) and is based on the power law behavior for the wavelet coefficients of fBm, namely,

$$\text{var}(d_j(n)) = (\sigma^2/2) V_{\varphi(H)} (2j)^{2H+1}$$

where $V_{\varphi(H)}$ is a constant that depends on the wavelet and the index H .

The simulated value of d is 0.4, which yields $H = 0.8$ based on the equation $H = d + 1/2$.

In Figures 10 and 11, panels b, d, and f are the log-log plot containing the rescaled range statistic \hat{R}/\hat{S} versus the log of the block size parameter τ . \hat{H} is obtained by estimating the slope. In the previous section the justification for the use of the rescaled range R/S as a statistic is given (i.e., $\hat{R}/\hat{S} \approx |\tau|^{\hat{H}}$). Although a careful asymptotic analysis of these two statistics for \hat{H} is apparently unavailable in the literature, the variability of these estimates as a function of sample size is clearly evident. Based on these studies a sample size of 3,000 or more points is clearly desirable to help stabilize the estimates. The sample size requirement is not an inordinate burden for infrared cameras that sample at a 30 (60) Hertz rate, because 3,000 samples can be obtained in 100 (50) seconds—a reasonable amount of time for many applications! However, more efficient statistical estimates with confidence intervals are clearly needed.

The wavelet estimates for the index \hat{H} in Figures 10 and 11 should be compared with the wavelet estimates in Figure 12. In all panels, the solid line connects the values of the variance at the respective scales ranging from 1 to 7, and the dotted lines are the least squares fit. Panels c, d, e, and f use the single wavelet D_{10} at all scales. The inflection point located at scale 2 in panels c, d, e, and f is also observed in the plots presented by Flandrin (Reference 22). He also discusses the rationale for this bend; the interested reader is referred to his paper. Panels b, d, and f use each member of the Daubechies wavelet family, D_{10} , D_4 , and D_2 in sequential order for two scales. The reduction in variability over the D_{10} only transforms is clearly evident. Again, the rationale for the reduction in variability is discussed by Tewfik and Kim (Reference 31). As the scales progress from fine to coarse the support of the wavelets needs to be adjusted to match the decrease in sample size at each scale.

Because any measurement obtained from an infrared camera detector will include both the $1/f$ -type noise depending on the detector material properties and other measurement-induced noise (e.g., analog-to-digital conversion, quantizing effects), it is reasonable to expect the periodogram to be corrupted with these noises. If the *a priori* knowledge of the spectral density of the measurement noise is unknown, then the problem becomes one of jointly measuring signal and noise. Wornell does address the problem by postulating an

additive model of a $1/f$ signal corrupted by stationary white Gaussian noise (Reference 12). In Figure 13, the simulated additive model sample paths are illustrated in panels a and c with corresponding d values of 0.4 and -0.4. The noise variance is equal to 4 in panel a and 0.0036 in panel c. Panels a, b, c, and d in Figure 12 should be compared with the panels a, b, e, and f in Figure 2. The main effect of the noise is to alter the rolloff rate in the high-frequency interval in the periodogram. The accumulated variance obtained from the sample paths $B_H(t)$ in panels a and c is plotted in panels e and f. The increase in the variance is another characteristic of persistent and antipersistent behavior.

Besides the index H , the other two parameters in the fractional Brownian model are the mean μ and the variance σ . These parameters will completely characterize fBm provided the marginal distributions of the increments $\nabla B_H(t)$ are Gaussian.

While the marginal distributions of the measured Amber camera data will probably never exactly match this standard, any respectable model identification procedure should define the degree of approximation.

Fortunately some graphical techniques exist to examine the marginal distributions. Figures 14 and 15 exhibit three methods found in *S-PLUS*. In Figure 14 the first four panels contain Q-Q plots. A Q-Q plot can be used to compare the degree of agreement between two empirical distributions or can be used to compare the empirical quantiles with the quantiles from an ideal distribution. A Q-Q plot is a plot of the ordered data y_i from the sample $\{x_0, \dots, x_{N-1}\}$ versus the normal quantiles $y_{p_i} = \Phi^{-1}(p_i)$, where $p_i = (i - 1/2)/N$, $i = 1, 2, \dots, N$, and Φ^{-1} is the inverse of the standard normal distribution (Reference 37). If the shape of the marginal distributions for the increments $\nabla B_H(t)$ is approximately normal, even in the tails, then the empirical quantile sample values will approximate the normal line. The Q-Q plots for the increments in panels a and c are linear even in the tails, so the Gaussian hypothesis for the marginal distribution as simulated by the Hosking ARIMA(0,d,0) model is reasonable. Clearly, the Q-Q plots for the sample paths are quite different with the persistent model exhibiting a radical departure from normality.

Panels e and f illustrate how the variance influences the range or excursion of the sample path:

$$R(\tau) = \max_{1 \leq t \leq \tau} X(t, \tau) - \min_{1 \leq t \leq \tau} X(t, \tau)$$

The Hosking fGn ARIMA(0,d,0) model does not constrain the variance to any particular value in the Gaussian generator, and for modeling purposes it is useful to have the variance as an extra degree of freedom.

Figure 15 shows the histograms and density estimates for the increments and sample paths. The agreement among the three estimates of distribution shape is quite good. Of course, any of these exploratory tools that are used to measure the shape are not a substitute for other tests for normality.

Figures 16 and 17, respectively, exhibit correlation functions between two different realizations of fBm and their associated increments. In Figure 16 panels c and f are the autocorrelations for the corresponding fBm sample paths in panels a and b. The positive coefficients and slow decay of the autocorrelation functions is one of the distinctive characteristics of processes with a spectral density like ARIMA(0,d,0) $d < 0$. Most traditional time-series analysis has been concerned with the property that observations separated by a long time span are nearly independent. These types of processes have correlation functions that are typically like those in Figure 17, panels c and d. Panels d and e are the corresponding cross correlations (with negative and positive lags) between the fBm in panels a and b. Panels d and e basically illustrate a small but persistent degree of long-term negative correlation, which is consistent with the apparent degree of cyclical behavior in the two sample paths. By contrast the cross-correlation plots for the increments indicate a total lack of correlation between the increments.

Figure 18 illustrates the analysis and synthesis processing versatility of the wavelet transform (see Figure 1). Panel a is the original signal fBm sample derived from a Hosking ARIMA(0,-0.4,0) model; panels b, d, and f are the detail coefficients $d_j(n)$ $j = 1,2,3$; and panels c and e are the approximation coefficients $a_j(n)$ $j = 2,3$. Panels g and h represent the resulting signal after wavelet synthesis, except that only selected scales from either the approximation coefficients $a_j(n)$ or the detail coefficients $d_j(n)$ are used. Panel g is the signal that results from reconstructing from scale e; i.e., only the coefficients $d_j(n)$ $j = 3$ are used for synthesis. Note how the density of noise in panel g is reduced from that in panel a. Panel h is the signal that results from reconstructing from scales b, d, and f; i.e., only the coefficients $d_j(n)$ $j = 1,2,3$, are used for synthesis. As expected, now the reconstructed signal h only has noise—the low-frequency drift has been filtered out of the signal.

AMBER CAMERA TEST RESULTS

In this section some pixel data taken from an Amber³ AE 4128 imaging system are tested to determine whether the fBm hypothesis is reasonable. The Amber camera is a 128 by 128 indium antimonide (InSb) staring array that operates at midwave infrared wavelengths of 3 to 5.5 μm . The imaging system includes an FPA, a transimpedance amplifier (TIA), a pour-filled dewar, an f3 lens, and an electronics unit for camera control.

Before the test the vacuum was pumped down to 10^{-5} torr. The camera lens was located about 1 inch from the blackbody, which was set at a constant temperature of 20°C during the measurements. The blackbody has a 4- by 4-inch surface area and is interfaced to an EO Industries blackbody temperature controller. The blackbody and temperature controller are accurate to $\pm 0.01^\circ\text{C}$. Two sets of measurements were conducted. Each distinct set was quantized to 12 bits of sampled data from the array. The first measurements consisted of two different sets of image sequences, namely, a burst set that contained 1,024 images with a sampling period of 1.4649 seconds, and long-term measurement set that contained 800 images with a sampling period of 60.6 seconds. The burst data was taken prior to each extended measurement. The dewar was filled with liquid nitrogen at the beginning of each test and was not refilled during the 13.5 hours of each test. This extended period without any refill is within the Amber guidelines for camera operation; however, saturation was clearly evident well beyond the 800 images retained in the long-term measurements database.

The second set of measurements required modifying the digital memory buffers so that the transfer rate from the array elements to the storage memory was commensurate with the maximum sampling rate of the array, which is 54 Hertz. Because the original memory buffers that were used for the data transfer from the array were designed for another task, to achieve the 54 Hertz rate a compromise solution was designed by Douglas Lamb of the Advanced Signal Processing Branch at NAWCWPNS China Lake. He was able to sample a 16- by 16-element subarray at the maximum rate. This data set, called the 54 Hertz set, is discussed in the final paragraphs of this section.

Table 3 lists the key camera parameter settings that were used during all of the tests.

In both Figures 19 and 20, the panels labeled "camera data" are the time-sampled output from an individual pixel on the Amber camera array. In each of these plots, the horizontal axis represents the number of samples, and the vertical axis is a gray scale.

³ AMBER Engineering, Inc., 5756 Thornwood Drive, Goleta, California, 93117-3802.

TABLE 3. Camera Parameter Settings.

| Camera parameters | Setting |
|-------------------|---------|
| TIA gain | 3 |
| TIA offset | 0 |
| Integration time | 32 |
| Frame rate | 54 |
| Global gain | 1 |
| Global offset | 0 |

The purpose of the panel plots in Figure 19 is to illustrate that the estimate of the Hurst index H can be extremely sensitive to the number of samples. Panel a is a fBm with a Hosking ARIMA(0,0.3,0) model, and panel b is the periodogram with the dotted line representing least squares fit for the estimate of H . The estimate is in good agreement with the proper value. Panel c is a segment of the fBm in panel a that is selected for its bow, which is a good approximation to the burst data. Panels d and f are the associated periodograms, both of which give a value for the index H that differs from the value in panel b. Of course, the estimate for H in panel d is clearly wrong! By way of comparison the fracdiff program with the panel c sample was able to estimate H correctly. Three lessons are illustrated in Figure 19. First, sample size is important. Second, the periodogram may not always be a reliable estimator of the index \hat{H} , especially if the sampled data set is too small. Third, the noise does influence the high-frequency values of the periodogram in a manner similar to that predicted in Figure 13. Unfortunately, no clear guidelines exist about these matters, other than basic Fourier estimates for the maximum and minimum frequency band that must be measured to obtain the best estimate of the index \hat{H} . Obviously, the lowest frequency f_{\min} is determined by $1/T$ where T is the total sample time, so a larger value of T means a lower frequency. The first two entries in Table 4 are the parameters for the sampled data sets, and the last two entries are the minimum and maximum frequencies in the measured frequency band. Here Δt is the sampling interval. The first two rows represent the burst and long-term data sets, respectively, while the last three rows are the parametric values. A 60-Hertz sampling rate is assumed.

TABLE 4. Fourier Sampling Parameters.

| Number of samples | Δt , seconds | f_{\min} , Hertz | f_{\max} , Hertz |
|-------------------|----------------------|--------------------|--------------------|
| 1024 | 1.4649 | 0.00066664 | 0.68264 |
| 800 | 60.6 | 0.00002062706 | 0.0165 |
| 3,600 | 0.016667 | 0.016667 | 60 |
| 7,200 | 0.016667 | 0.008333 | 60 |
| 360,000 | 0.016667 | 0.000167 | 60 |

In Figure 20, the variability of the statistic H due to data smoothing is illustrated. These changes can be anticipated by consulting Figure 2.

In Figure 21 panels a, c, and e are plots of 640 time-sampled values from pixels (10,9), (10,10), and (10,11), respectively, taken from the long-term measurements. Panels b, d, and f are the periodograms, and the index \hat{H} is the slope of the dotted line obtained by a least squares fit. The agreement among the indices is consistent with the hypothesis that the spatial noise on the Amber camera is fBm with a mean power law of $\frac{1}{f^{1.7321}}$. Table 5 includes estimates of the index \hat{H} taken over a larger sample of pixels.

In Figure 22 panels a, c, and e are plots of 640 time-sampled values from pixels (10,9), (10,10), and (10,11), respectively, taken from the long-term measurements.

Panels b, d, and f are the Q-Q plots for the increments. The spacing of the bars on in the Q-Q plots is caused partially by the coarseness of the quantization for the measured interval (i.e., the 12-bit quantization is spread over a larger range). Clearly the increments are well approximated by the Gaussian shape. The corresponding histograms and density estimates are shown in Figure 23 and clearly confirm the quantile plots prediction.

Panels a and c in Figure 24 are plots of 640 time-sampled values from pixel (10,10) taken from the long-term measurements. The other panels show the reasonable agreement among the Hurst, wavelet, and periodogram estimates for the index \hat{H} . The new addition is panel f, which is a plot of the correlation function for the increments. The Hosking fGn ARIMA(0,0,d,0) model predicts that the correlation coefficients will all be positive for $d > 0$ and for $d < 0$, and the coefficient will be negative and the follow the positive axis as a function of the lag. The Amber camera correlation is consistent with the antipersistent case, namely ($d < 0$) and should be compared with Figure 17, panels e and f. The agreement between the simulated fBm and the Amber camera in this case is excellent.

Figures 25 and 26 exhibit, respectively, the correlation functions between pixels (10,10) and (10,11) and their associated increments. In Figure 25 panels a and f are the autocorrelations for the spatial noise in panels c and b. The positive coefficients and slow decay of the autocorrelation functions is one of the distinctive characteristics of processes that the fBm simulation clearly exhibited in Figures 3 and 16. Thus, the observations separated by a long time span are more persistent and are clearly not negligible. Time series with the slow decay exhibit cycles and changes of level of all orders of magnitude—a description that matches both the Amber camera data and the fBm. Panels d and e, the corresponding cross correlations between panels a and b, illustrate a persistent degree of long-term positive correlation, which is consistent with the apparent degree of cyclical behavior in the two sample paths.

TABLE 5. Amber Camera Statistics.

| Pixel sample path statistics | | | | | Increments statistics | | | |
|------------------------------|------|------|------|-------|-----------------------|-----|-------|--------|
| (x,y) | Min | Max | Mean | Var | Min | Max | Var | H |
| (9,9) | 983 | 1017 | 998 | 44.43 | -9 | 8 | 8.02 | 0.3886 |
| (9,10) | 823 | 868 | 843 | 71.44 | -13 | 14 | 24.65 | 0.3324 |
| (9,11) | 942 | 978 | 959 | 52.45 | -8 | 10 | 8.12 | 0.3711 |
| (10,9) | 959 | 992 | 973 | 47.32 | -9 | 8 | 8.06 | 0.3594 |
| (10,10) | 844 | 878 | 859 | 45.99 | -10 | 11 | 9.98 | 0.3579 |
| (10,11) | 806 | 841 | 819 | 51.18 | -9 | 9 | 8.31 | 0.4035 |
| (11,9) | 1104 | 1141 | 1119 | 52.12 | -9 | 7 | 8.59 | 0.3723 |
| (11,10) | 856 | 890 | 869 | 47.11 | -8 | 10 | 9.94 | 0.3798 |
| (11,11) | 948 | 983 | 965 | 50.36 | -10 | 10 | 9.62 | 0.3612 |
| (20,21) | 889 | 922 | 904 | 46.23 | -9 | 10 | 7.94 | 0.3779 |
| (21,20) | 733 | 775 | 750 | 52.68 | -13 | 18 | 17.02 | 0.2975 |
| (21,21) | 813 | 848 | 827 | 44.88 | -9 | 9 | 9.17 | 0.332 |
| (21,22) | 817 | 853 | 831 | 48.55 | -10 | 9 | 8.96 | 0.4241 |
| (22,21) | 910 | 943 | 924 | 49.33 | -9 | 9 | 8.42 | 0.4252 |
| (32,32) | 912 | 946 | 928 | 50.08 | -11 | 11 | 9.52 | 0.3994 |
| (20,64) | 899 | 935 | 915 | 50.85 | -8 | 9 | 8.23 | 0.371 |
| (21,63) | 877 | 910 | 893 | 45.05 | -9 | 10 | 10.86 | 0.3749 |
| (21,64) | 938 | 973 | 954 | 55.48 | -10 | 10 | 9.34 | 0.3538 |
| (21,65) | 1049 | 1085 | 1064 | 54.38 | -10 | 10 | 11.03 | 0.3585 |
| (22,64) | 850 | 890 | 868 | 51.12 | -10 | 8 | 9.33 | 0.3722 |
| (32,64) | 909 | 950 | 928 | 56.93 | -13 | 13 | 16.38 | 0.3477 |
| (10,110) | 496 | 536 | 511 | 58.33 | -9 | 11 | 11.17 | 0.3897 |
| (20,105) | 657 | 693 | 671 | 43.01 | -11 | 9 | 10.12 | 0.3478 |
| (21,104) | 577 | 610 | 593 | 42.93 | -11 | 11 | 10.98 | 0.3482 |
| (21,105) | 602 | 637 | 615 | 39.07 | -9 | 9 | 8.29 | 0.3263 |
| (21,106) | 419 | 456 | 436 | 44.35 | -10 | 9 | 9.32 | 0.3355 |
| (22,105) | 673 | 708 | 686 | 47.03 | -8 | 7 | 7.8 | 0.3355 |
| (32,95) | 944 | 979 | 959 | 50.13 | -11 | 12 | 11.75 | 0.3437 |
| (63,21) | 1301 | 1346 | 1318 | 80.42 | -11 | 12 | 14.52 | 0.3472 |
| (64,20) | 991 | 1028 | 1007 | 55.25 | -13 | 11 | 9.93 | 0.3573 |
| (64,22) | 1025 | 1059 | 1040 | 50.31 | -10 | 10 | 9.25 | 0.3521 |
| (64,32) | 1105 | 1143 | 1122 | 48.96 | -9 | 10 | 10.41 | 0.3907 |
| (65,21) | 1213 | 1249 | 1229 | 52.78 | -8 | 13 | 8.22 | 0.3827 |
| (63,64) | 1110 | 1150 | 1125 | 49.16 | -9 | 10 | 8.4 | 0.3766 |
| (64,64) | 1222 | 1256 | 1237 | 48.49 | -10 | 10 | 9.82 | 0.389 |
| (64,63) | 1289 | 1330 | 1306 | 57.88 | -17 | 14 | 22.91 | 0.3175 |
| (64,65) | 1316 | 1353 | 1333 | 51.59 | -9 | 9 | 10.95 | 0.3994 |
| (65,64) | 1239 | 1275 | 1255 | 52.81 | -9 | 10 | 10.21 | 0.4079 |
| (64,95) | 1191 | 1234 | 1209 | 53.26 | -11 | 11 | 12.54 | 0.3747 |
| (64,104) | 945 | 981 | 960 | 49.31 | -9 | 8 | 8.17 | 0.3781 |
| (64,105) | 1208 | 1244 | 1223 | 52.87 | -9 | 9 | 8.67 | 0.4117 |
| (64,106) | 970 | 1003 | 986 | 47.03 | -10 | 8 | 9.64 | 0.3134 |
| (65,105) | 1313 | 1349 | 1329 | 51.63 | -10 | 11 | 10.52 | 0.3784 |
| (95,25) | 1351 | 1387 | 1367 | 56.48 | -11 | 9 | 9.18 | 0.4293 |
| (95,32) | 1092 | 1126 | 1107 | 53.18 | -9 | 8 | 9.74 | 0.3624 |
| (104,21) | 1204 | 1239 | 1219 | 48.57 | -10 | 8 | 8.83 | 0.3756 |
| (105,20) | 1016 | 1052 | 1032 | 50.73 | -8 | 12 | 8.57 | 0.3646 |
| (105,21) | 1145 | 1181 | 1161 | 48.38 | -10 | 9 | 9.47 | 0.3158 |
| (105,22) | 1065 | 1102 | 1082 | 48.19 | -9 | 9 | 9.16 | 0.3878 |
| (106,21) | 1220 | 1256 | 1238 | 48.28 | -15 | 12 | 14.05 | 0.3812 |
| (110,10) | 1177 | 1219 | 1197 | 59.84 | -16 | 16 | 20.98 | 0.32 |
| (95,64) | 1121 | 1158 | 1139 | 53.91 | -10 | 10 | 10.58 | 0.3575 |
| (104,64) | 1146 | 1181 | 1164 | 53.67 | -10 | 9 | 10 | 0.3602 |
| (105,63) | 1258 | 1294 | 1275 | 53.21 | -9 | 11 | 9.54 | 0.4362 |
| (105,64) | 1170 | 1206 | 1187 | 56.02 | -10 | 8 | 9.44 | 0.3832 |
| (105,65) | 1319 | 1353 | 1334 | 52.86 | -10 | 12 | 10.66 | 0.3521 |
| (106,64) | 1043 | 1080 | 1058 | 45.57 | -8 | 10 | 9.78 | 0.3602 |
| (95,95) | 1329 | 1367 | 1347 | 53.95 | -9 | 10 | 13.12 | 0.3664 |
| (104,105) | 1274 | 1311 | 1289 | 48.3 | -11 | 10 | 8.93 | 0.3603 |
| (105,104) | 987 | 1026 | 1002 | 54.38 | -11 | 9 | 9.82 | 0.3558 |
| (105,105) | 1158 | 1190 | 1172 | 47.6 | -9 | 9 | 7.39 | 0.3516 |
| (105,106) | 966 | 1000 | 982 | 47.29 | -10 | 10 | 9.32 | 0.3459 |
| (106,105) | 1192 | 1229 | 1210 | 50.82 | -10 | 11 | 9.75 | 0.3166 |
| (110,110) | 1028 | 1060 | 1042 | 50.05 | -10 | 9 | 10.04 | 0.3765 |

Correlation functions that are typically like those in Figures 26 panels c and d mean that observations separated by a long time span are nearly independent. The cross correlation plots for the increments indicate a total lack of correlation between the increments. These panels again show a remarkable agreement with the correlation functions increments for fBm plotted in Figure 17 in the same panels.

Table 5 contains the summary statistics from 63 Amber camera pixels from the 128 x 128 array. Each pixel sample is a discrete time sequence with 640 samples. The first column in the table represents the pixel coordinates with indices

$$[a_{i,j}] \quad i = 0, \dots, 127, j = 0, \dots, 127$$

The statistics are obtained for each pixel with its discrete time sequence of 640 samples. The statistics for the columns labeled "sample path" are for these sequences, and the increments statistics are obtained after differencing the time sequences by applying the difference operator defined in the FBM, Wavelets, and ARIMA Models section. The columns labeled min, max, mean, and var are the minimum values, the maximum values, the sample mean, and the sample variance for each discrete pixel time sequence and the corresponding increments. The column labeled H is the fBm index H estimate discrete time sequence.

Table 6 presents the statistics for each of the columns in Table 5. As is evident the index H has a mean value of 0.3660, yielding a exponent of 1.732 for the fBm spectrum. The mean value of the variance for the fBm process is 10.52. It is more variable because some of the pixels have some outliers, as an examination of the maximum and minimum values suggests. Of course the outliers' presence should be checked by computing the Q-Q plots. Recall that the variance for fBm governs the marginal distribution for the increments.

TABLE 6. Amber Camera Global Statistics.

| | Pixel sample path statistics | | | | Increments statistics | | | |
|----------|------------------------------|--------|---------|-------|-----------------------|-------|-------|--------|
| | Min | Max | Mean | Var | Min | Max | Var | H |
| Mean | 1014.5 | 1050.8 | 1030.38 | 51.19 | -10.1 | 10.13 | 10.52 | 0.366 |
| Variance | 46005.6 | 46140 | 46206.7 | 36.98 | 3.23 | 3.89 | 11.11 | 0.0009 |
| Std Dev | 214.49 | 214.8 | 214.96 | 6.08 | 1.8 | 1.97 | 3.33 | 0.0293 |
| Min | 419 | 456 | 436 | 39.07 | -17 | 7 | 7.39 | 0.2975 |
| Max | 1351 | 1387 | 1367 | 80.42 | -8 | 18 | 24.65 | 0.4362 |

In Figure 27 the panels a, c, and e are the time-sampled output from an individual pixel on the Amber camera array. In each of these plots the horizontal axis represents the number

of samples, and the vertical axis is a gray scale. All of the data in Figures 27, 28, 29, 30, and 31 were sampled at 54 Hertz.

In Figure 27 panels a, c, and e are time samples from the Amber camera data from three adjacent pixels on the same row. Panels b, d, and f are the periodograms, and the index \hat{H} is the slope of the dotted line obtained by a least squares fit. The agreement among the indices is consistent with the hypothesis that the spatial noise on the Amber camera is fBm. The estimates for \hat{H} are 0.385304, 0.158828, and 0.356435, respectively, for pixels (8,7), (8,8) and (8,9). Using the formula $\alpha = 2\hat{H} + 1$ yields a power spectrum inversely proportional to the frequency $f^{-\alpha}$ with values 1.7706, 1.3176, and 1.7128, respectively, for pixels (8,7), (8,8) and (8,9). Note that pixel (8,8) exhibits some degree of flicker noise.

Panels b, d, and f in Figure 28 are the Q-Q plots for the increments. The spacing of the bars on in the Q-Q plots is partially due to the coarseness of the quantization for the measured interval (i.e., the 12-bit quantization is spread over a larger range). Clearly the increments are well approximated by the Gaussian shape. The corresponding histograms and density estimates, shown in Figure 29, clearly confirm the quantile plots prediction.

As a confirmation of the predicted behavior of wavelet processing on fBm, Figures 30 and 31 illustrate the wavelet transform ability to "decorrelate or whiten" fBm as predicted by Flandrin (Reference 22). Panels b, d, and f in each of these figures are plots of the detail coefficients $d_j(n)$ $j = 1, 2, 3$ for the corresponding wavelet transform. In each figure panel c is the correlation evaluated using the third scale detail coefficients $d_3(n)$. Panel c in each of these figures compares very favorably with the simulated counterparts in Figures 6 and 8. These results clearly support the Flandrin's claim.

CONCLUSIONS

The most important contribution of this report is the demonstration that Daubechies wavelets do filter the fixed pattern noise in a predictable fashion. This claim is based on the results obtained by applying her wavelet transform to the temporal fixed pattern noise measurements taken by an InSb Amber FPA. The $1/f$ character of fixed pattern temporal noise measured in the 3- to 5.5- μm region by a 128 by 128 InSb staring array has been identified as fractional Brownian motion. Wavelet processing successfully decorrelated the fixed pattern noise. The results of this report can also serve as basis for fixed pattern noise models that can be used in missile simulations to test various detection and nonuniformity

compensation algorithms. All three sets of data were measured during this study, and each exhibits the presence of long-term correlation, which is a necessary condition, but not sufficient for having a $1/f$ -type spectrum. The correlation of the three data sets is also predictably changed after the sets are wavelet-transformed. Again, the change in correlation is a necessary condition and is another confirmation of the fBm model.

An important implication of the wavelet characterization of fixed pattern noise is that it suggests an optimum detection strategy in imaging arrays. Presently, the optimum detection strategy in the presence of fixed pattern noise and clutter is a key unresolved problem. Although conventional detection algorithms will suffice for the white noise and shot noise present on these arrays, the fixed pattern noise requires novel techniques for optimum detection. The rationale for the detection of a point target in clutter proceeds as follows and is suggested by the radar methodology for this problem, which is well known and which, by analogy, suggests the following steps for infrared arrays. First, solve the detection problem when only fixed pattern noise is present by characterizing the noise on the array. Next, define an optimum detection algorithm. This paradigm is exactly parallel to standard processing that has been successfully used in radar-detector design. Next, formulate an adaptive detection algorithm recognizing the array noise limits. Then maximize the detection signal-to-clutter ratio.

This report provides a unified review of fractional Brownian motion, wavelets, and a low-frequency spectrum $1/f$ -type noise of the form $\omega^{-\alpha}$ $1 \leq \alpha \leq 2$. By comparison, most traditional noise processes are characterized by short-term correlation with rapid decay, whereas a noise sequence with a $1/f$ -type spectrum has a correlation function that decays very slowly and has nonzero values at long distances. It is our contention that the $1/f$ -type noise is a major contributor to array nonuniformity. Moreover, the long-term correlation structure of $1/f$ -type noise precludes the direct application of conventional point target detection algorithms.

The report characterizes the $1/f$ -type noise as fractional Brownian motion. Both the theory and the examples presented in the report show that wavelet transforms can transform a low-frequency, $1/f$ -type noise spectrum of the form $\omega^{-\alpha}$ $1 \leq \alpha \leq 2$ into a flat white-noise-type spectrum. In other words, the $1/f$ -type noise has been decorrelated. Decorrelation is important because it means that the wavelet transform acts as a simple $1/f$ filter. The demonstration that the wavelet transform decorrelates the fixed pattern noise means that the array nonuniformity has been reduced and standard detection algorithms for decorrelated white noise can be applied after the wavelet transform. The implications for point target detection in fixed pattern noise means that the noise on all conventional staring arrays, whether they be InSb, HgCdTe, or PtSi, can be decorrelated. Thus, the apparent lack of $1/f$ -type noise in the PtSi arrays would not be such an obvious major advantage,

because the $1/f$ -type noise on InSb and HgCdTe can be converted to white noise by wavelet processing.

The fractional Brownian motion model links the covariance of the sample path or time history as it evolves in time with its power spectrum. It is a parasimonious model (it depends on two parameters) for $1/f$ noise. In fact, one important feature of fBm is that it provides a model of how long-range correlation is directly related to the parameters of the spectrum. By comparison, most traditional noise processes are characterized by short-term correlation with rapid decay, whereas a noise sequence with a $1/f$ -type spectrum has a correlation function that decays very slowly and has nonzero values for long lags. While noise can be classified according to its power spectrum, it is important to consider the relation between the time domain and the frequency domain. An important implication of the fBm model is that the power spectrum (representing the frequency domain) is linked via the Fourier transform with the covariance (representing the time domain). This linkage predicts a time-dependent envelope for the maximum excursion of the sample path of each pixel as measured by the variance. This variance formula provides a link between spatial noise on the array and the time-varying noise associated with an individual pixel, because the model predicts that the measured responses of the individual pixels, which are observed by viewing a constant source, will eventually drift randomly away from their original nominal value. In fact, the power spectrum as measured by the periodogram of the individual pixels provides an excellent indicator of the type of spatial noise that will be present on the array, especially if the spatial noise is measured by the ratio of the sampled variance across the array divided by the sampled mean across the array. For example, if the spectrum is white, then this ratio for the spatial noise will be statistically constant, but if the spectrum is of the form $\omega^{-\alpha}$ with $1 \leq \alpha \leq 2$, then the ratio will increase at a rate that is directly related to the exponent α . In this sense temporal noise and spatial noise are not independent!

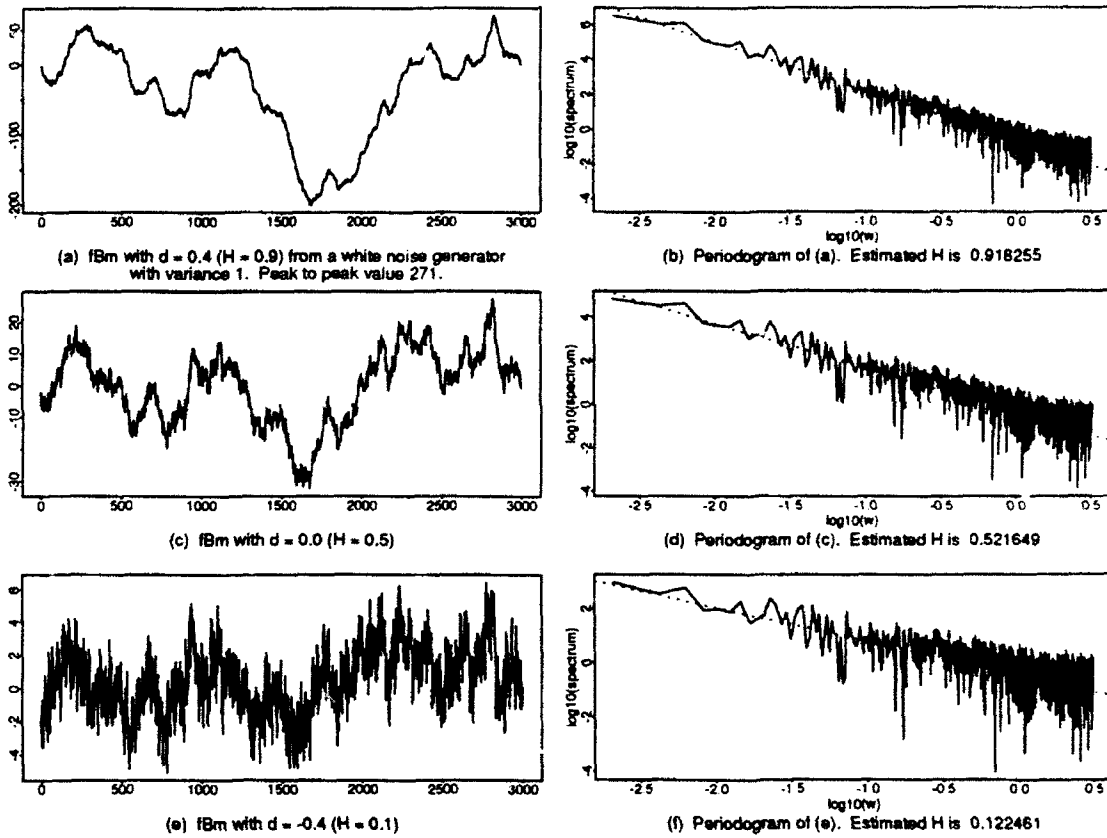


FIGURE 2. FBms and Their Periodograms.

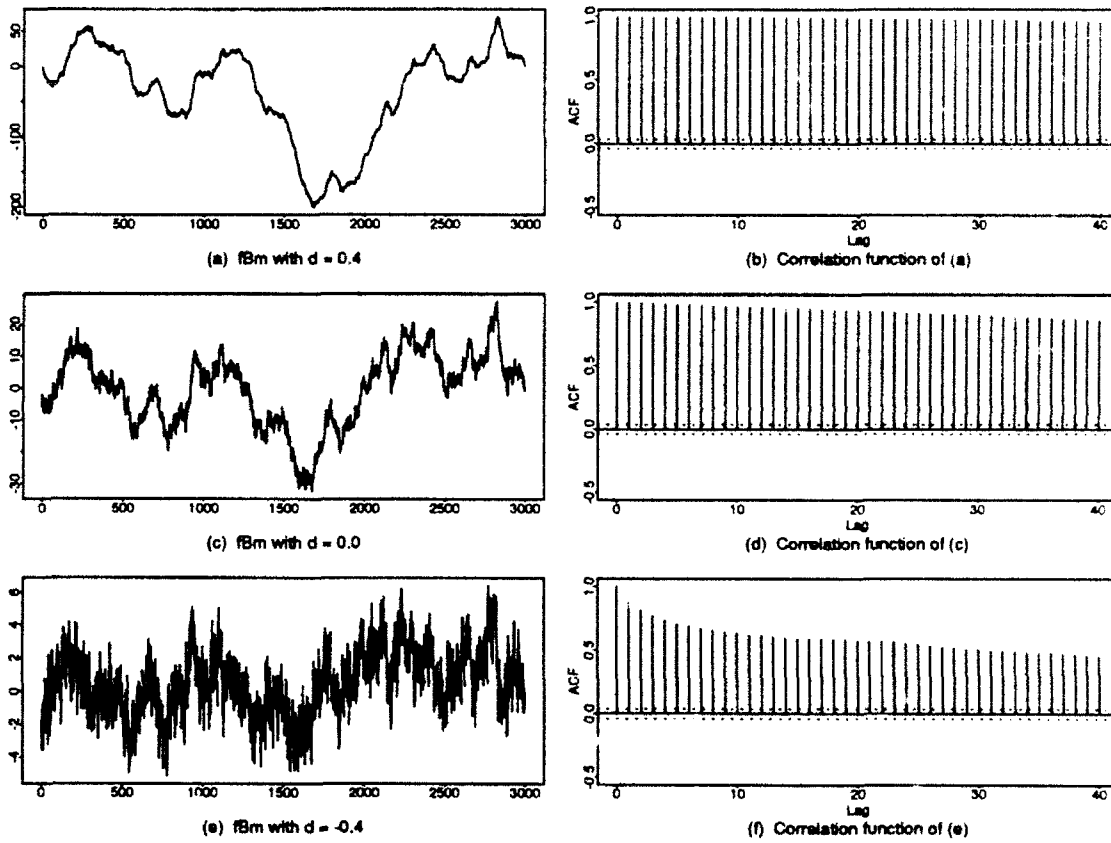


FIGURE 3. FBms and Their Autocorrelation Functions.

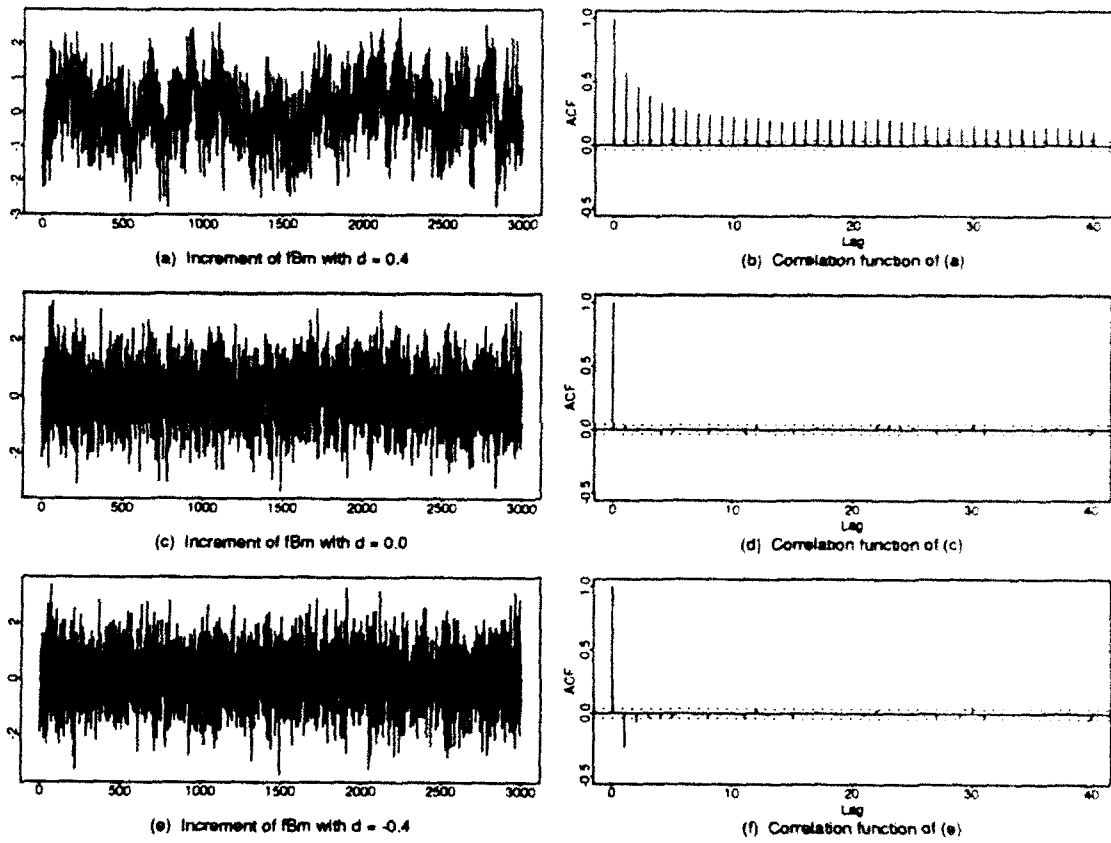


FIGURE 4. Increments of FBms and Their Correlation Functions.

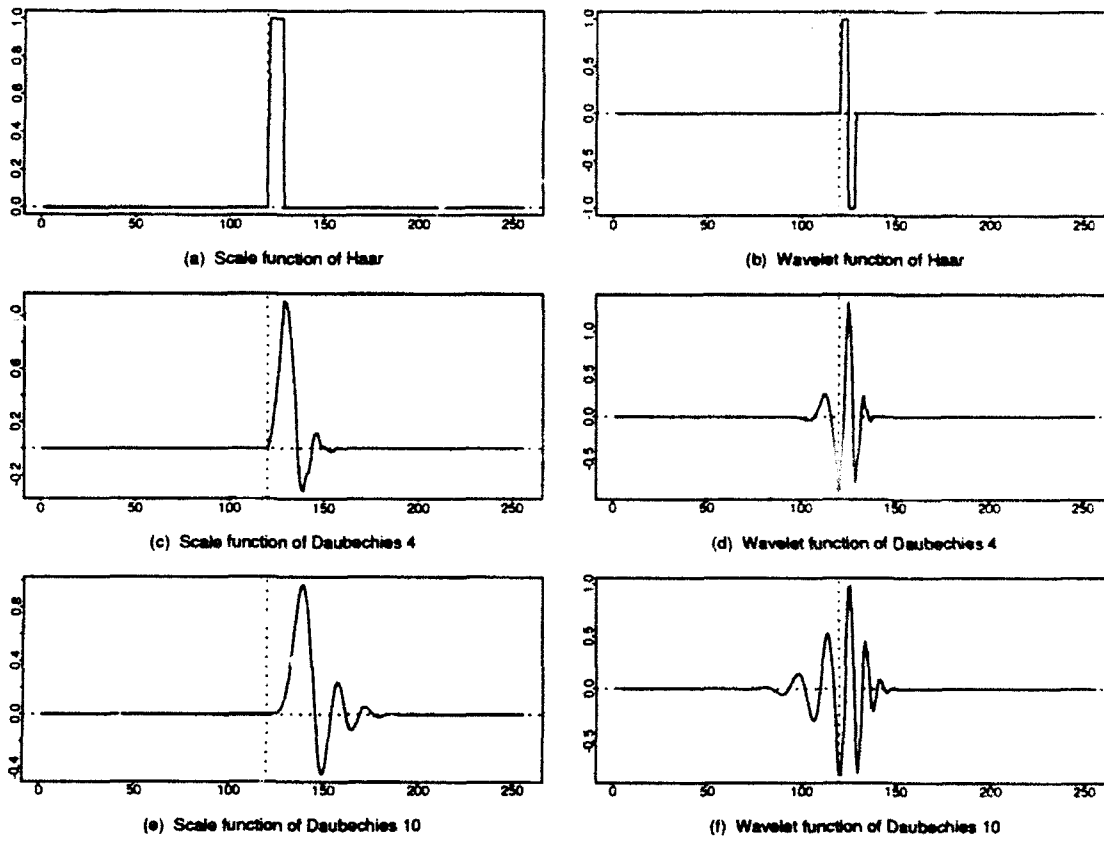


FIGURE 5. Scale and Wavelet Functions of Several Wavelets.

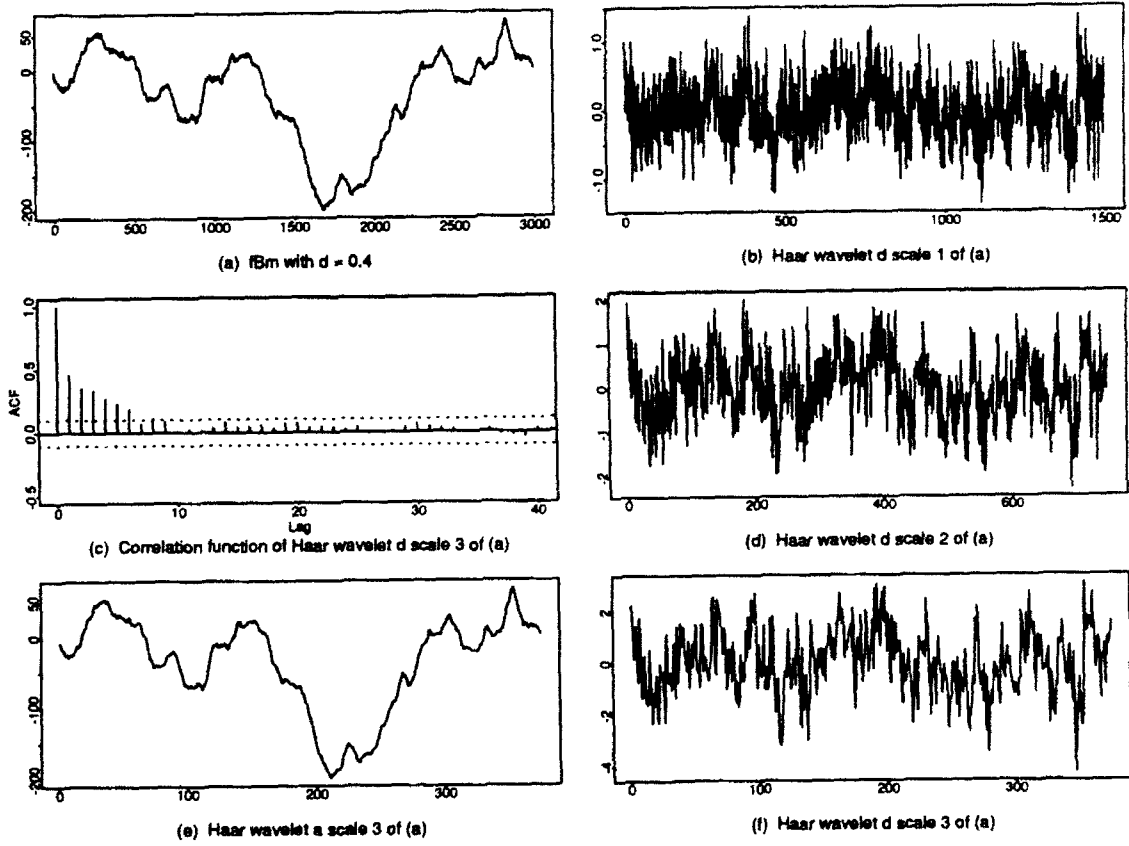


FIGURE 6. fBm With $d = 0.4$ and Haar Wavelet.

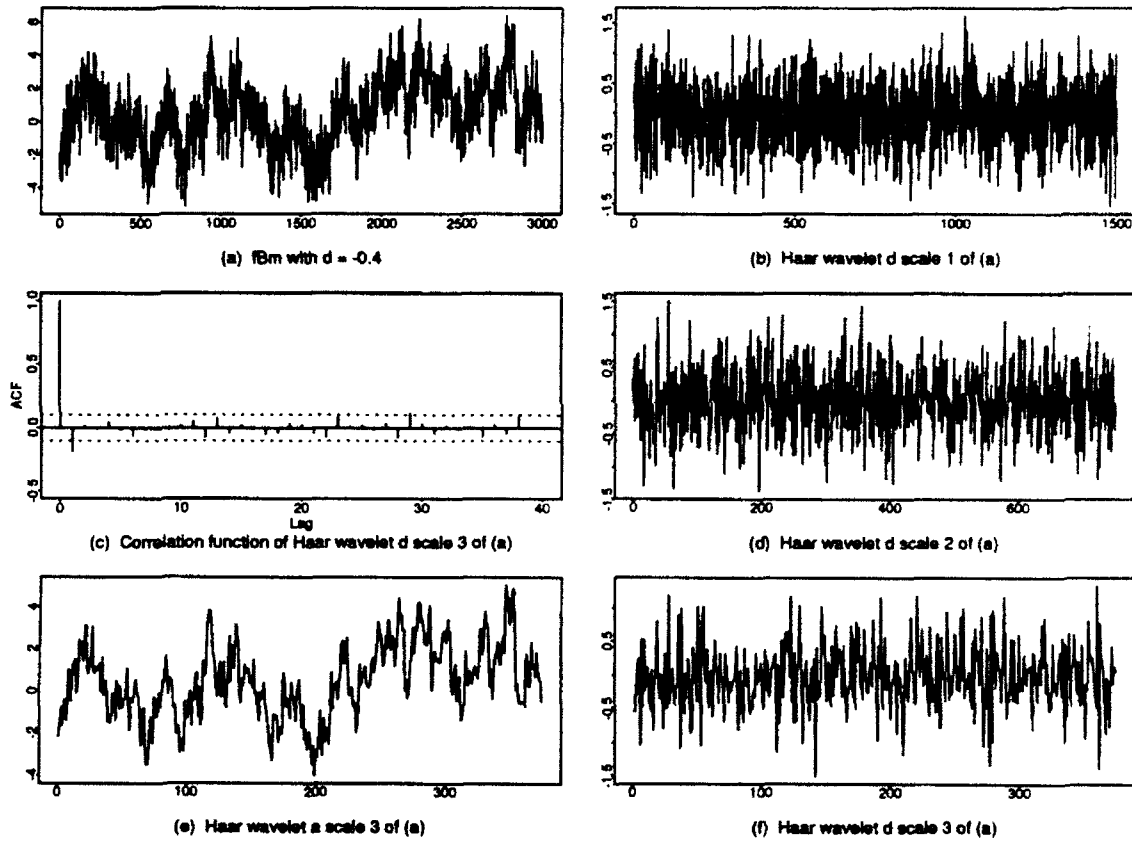


FIGURE 7. FBM With $d = -0.4$ and Haar Wavelet.

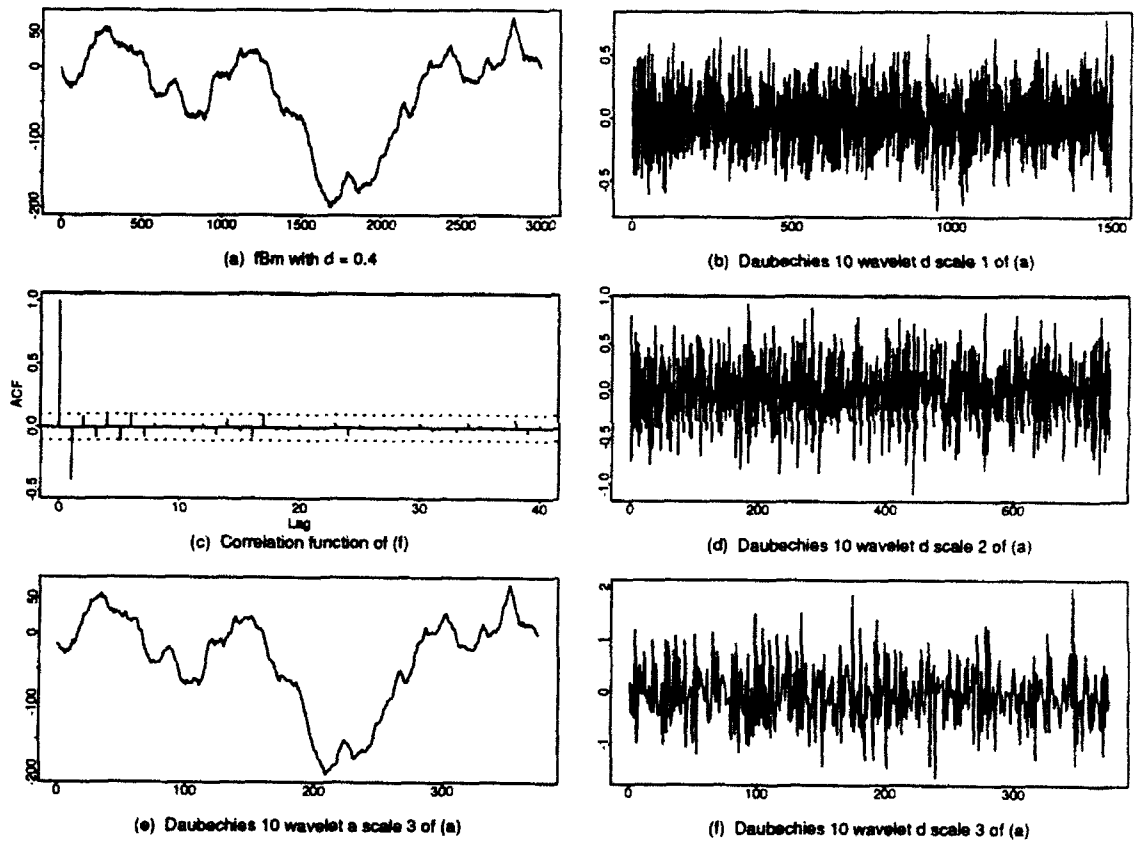


FIGURE 8. FBm With $d = 0.4$ and Daubechies 10 Wavelet.

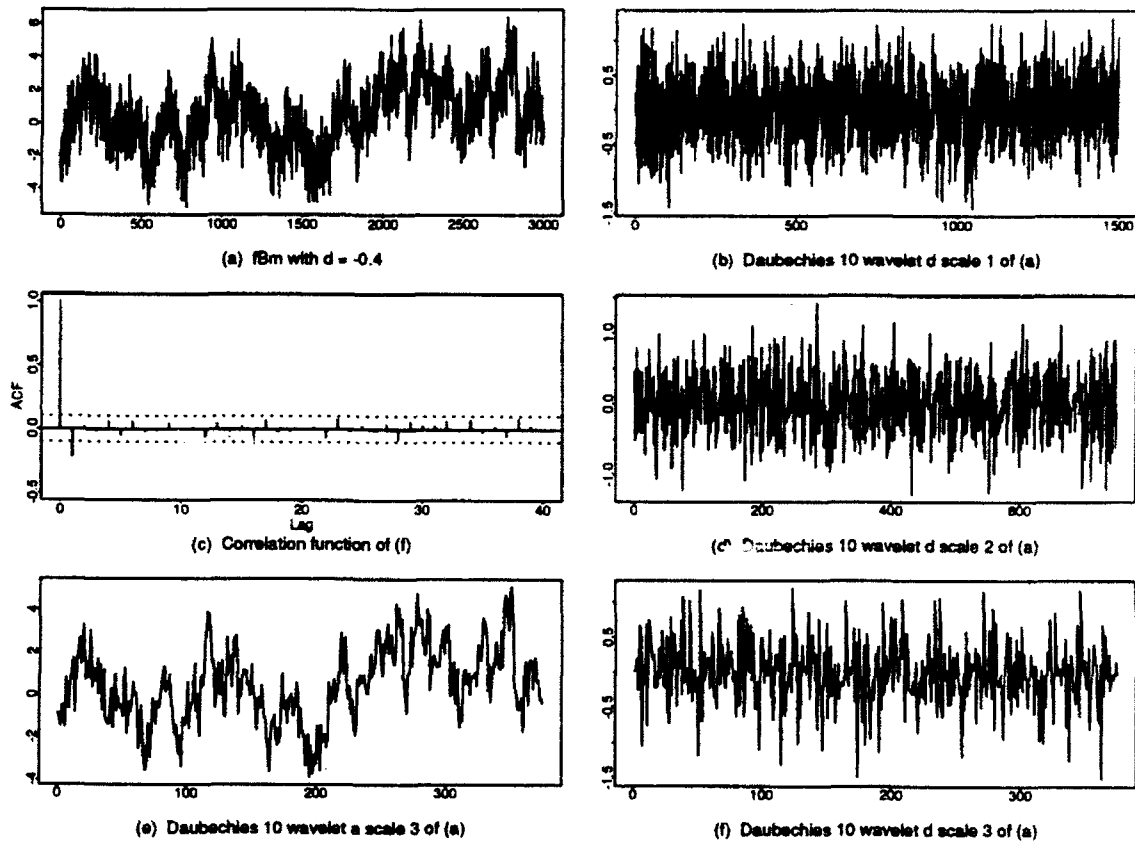


FIGURE 9. FBM With $d = -0.4$ and Daubechies 10 Wavelet.

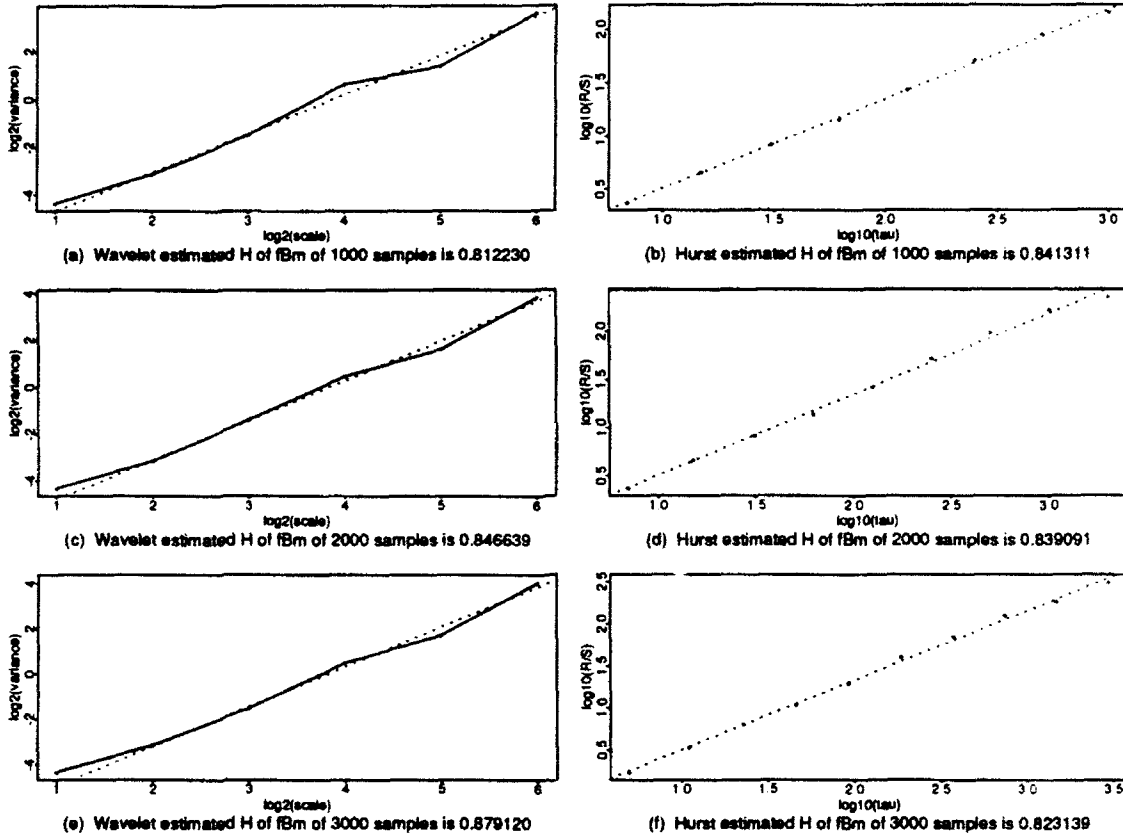


FIGURE 10. Estimation of H of fBm With $d = 0.4$ ($H = 0.9$) by Hurst Rescaled Range and Daubechies 10 Wavelet.

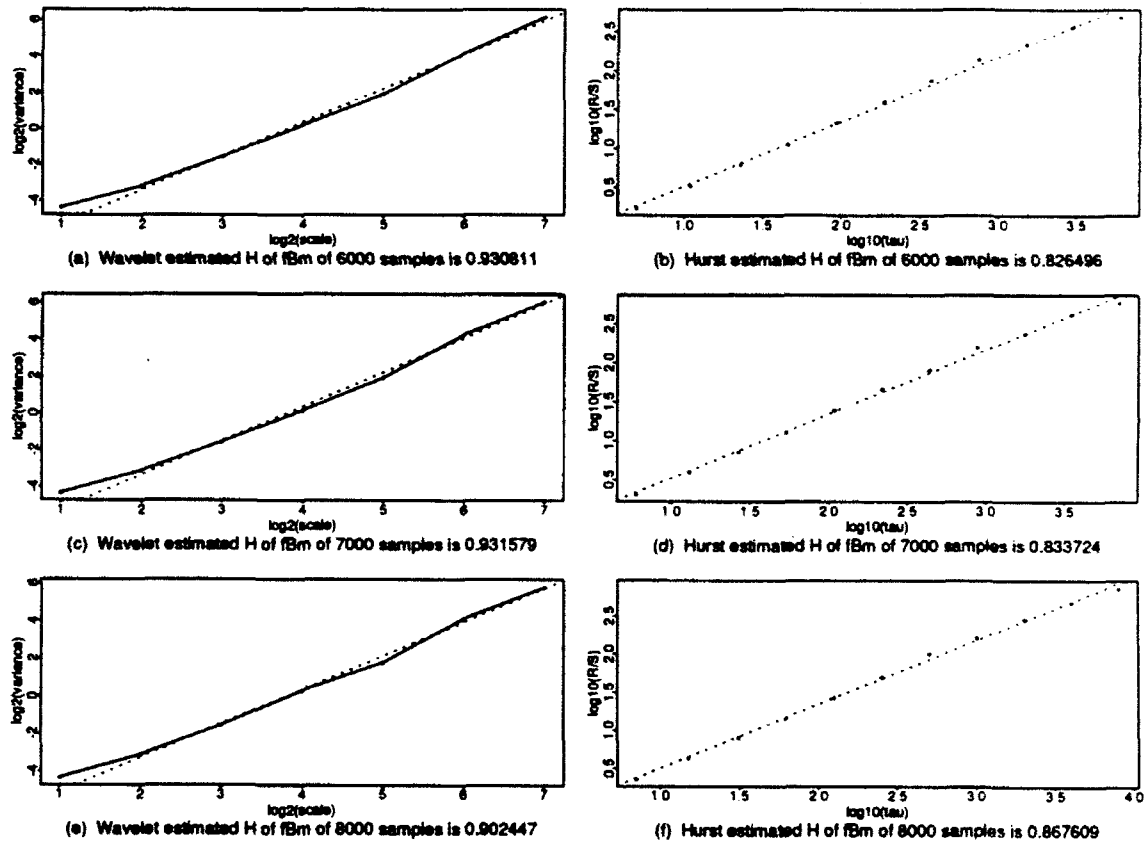


FIGURE 11. Estimation of H of fBm With $d = 0.4$ ($H = 0.9$) by Hurst Rescaled Range and Daubechies 10 Wavelet.

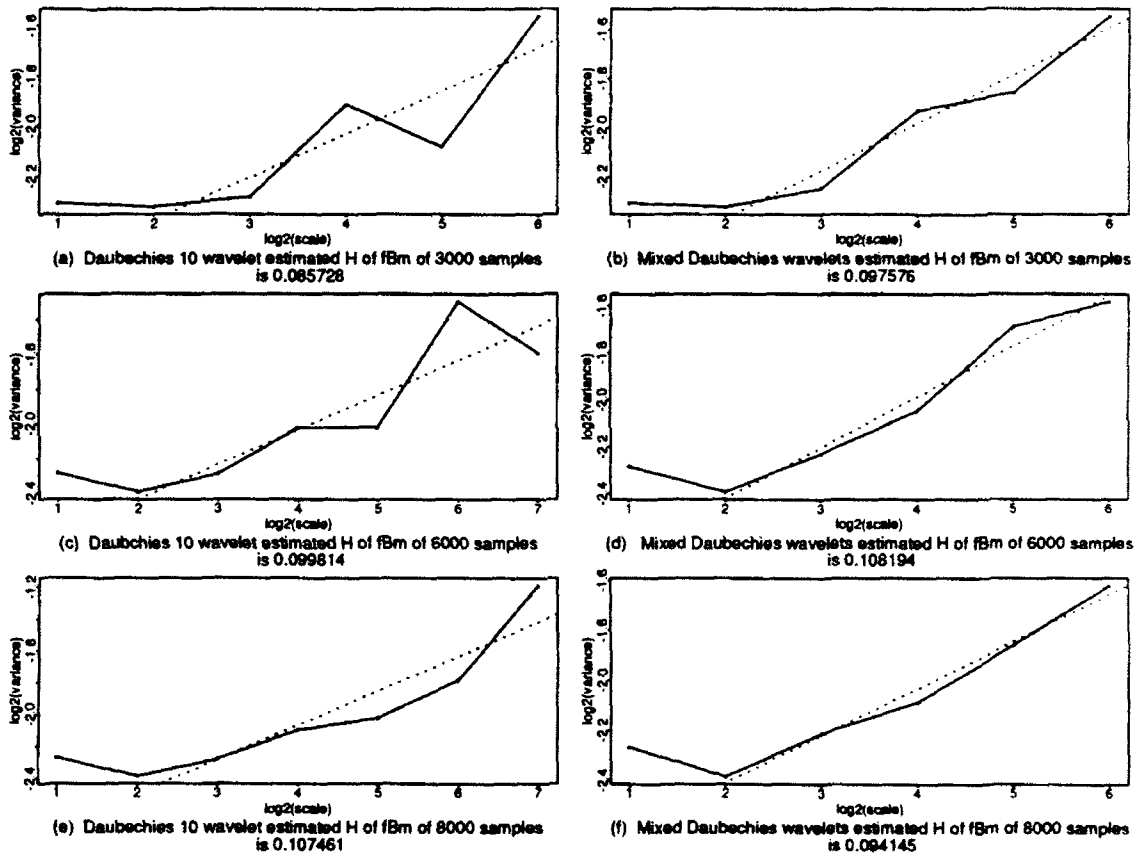


FIGURE 12. Estimation of H of fBm With $d = -0.4$ ($H = 0.1$) by Daubechies 10 and Mixed Daubechies Wavelets.

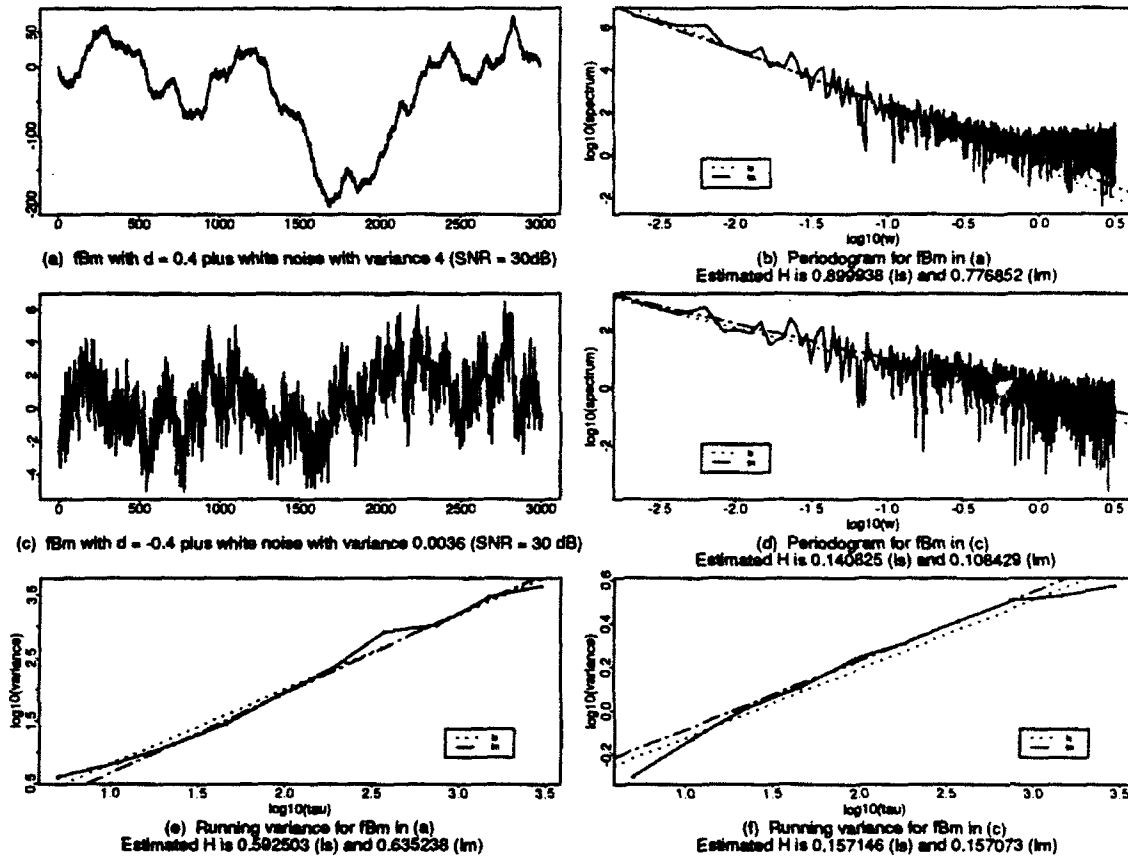


FIGURE 13. Sensitivity of fBm to Noise.

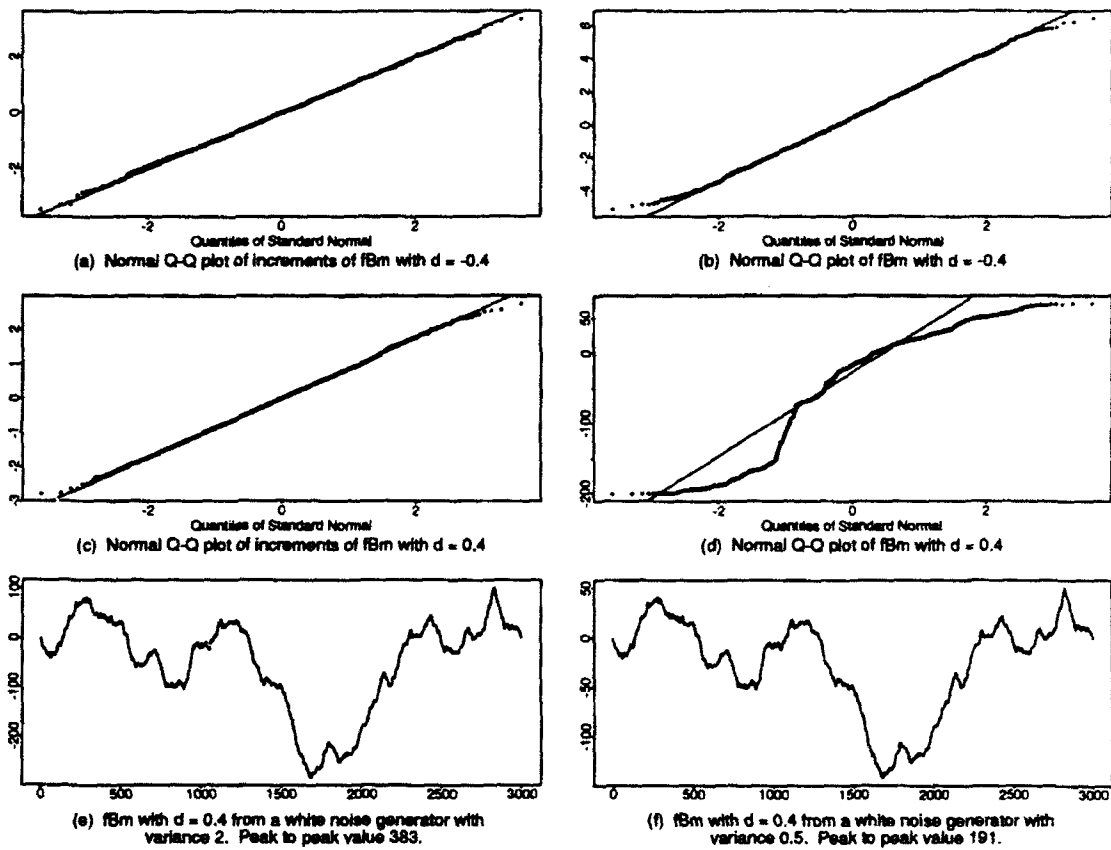


FIGURE 14. Normal Q-Q Plots and Variance Step Size Effect.

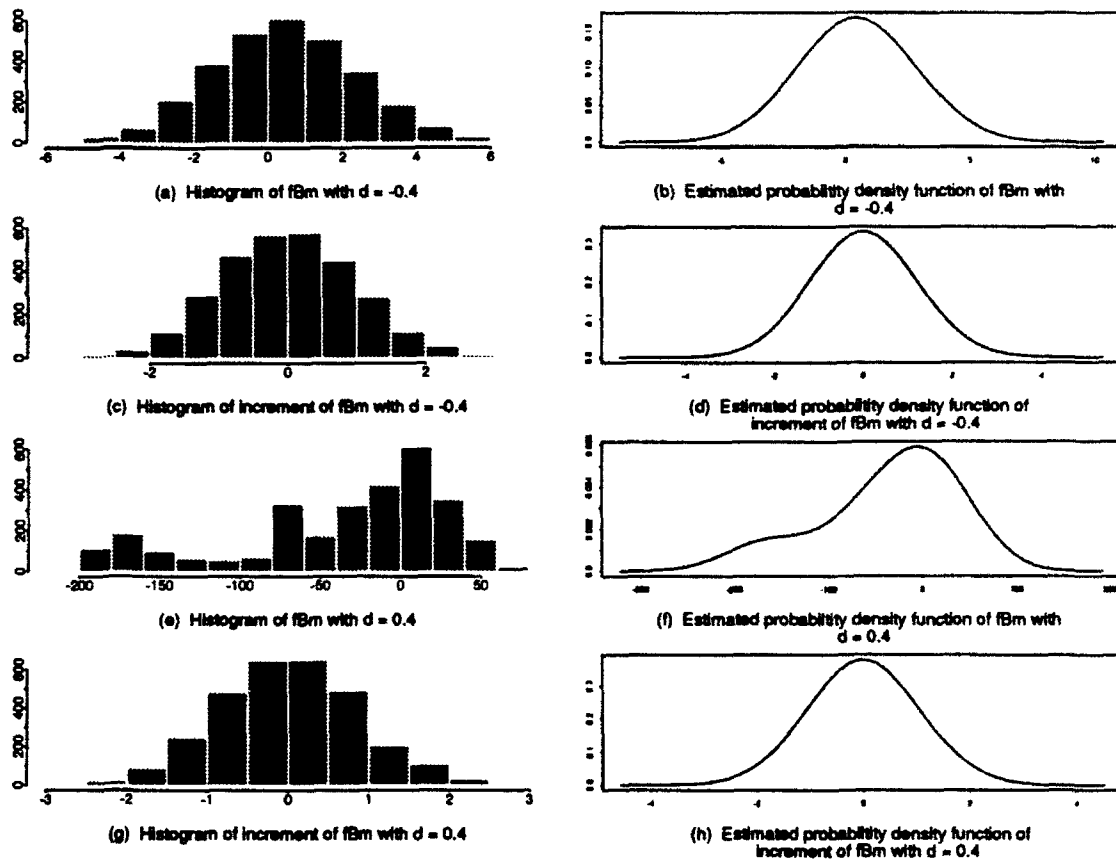


FIGURE 15. Histograms and Estimated Probability Density Functions of fBMs and Their Increments.

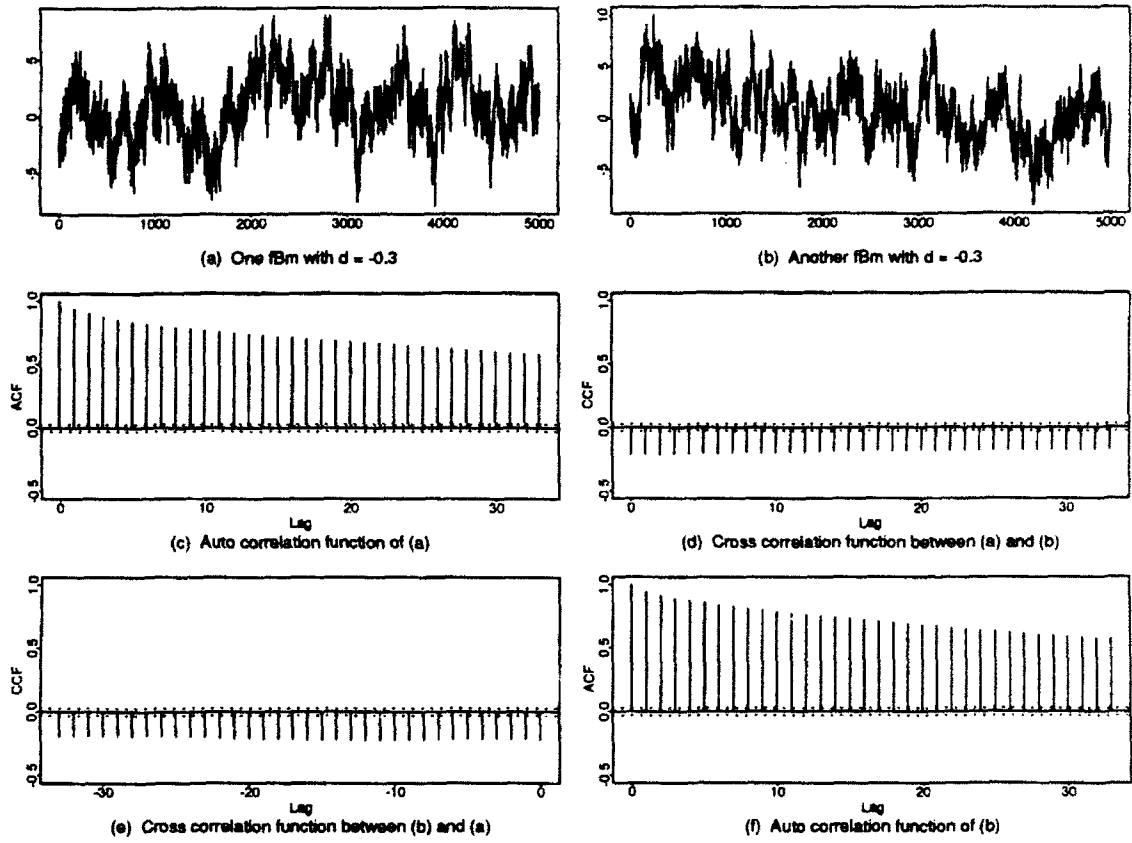


FIGURE 16. Correlation Functions Between fBms With $d = -0.3$.

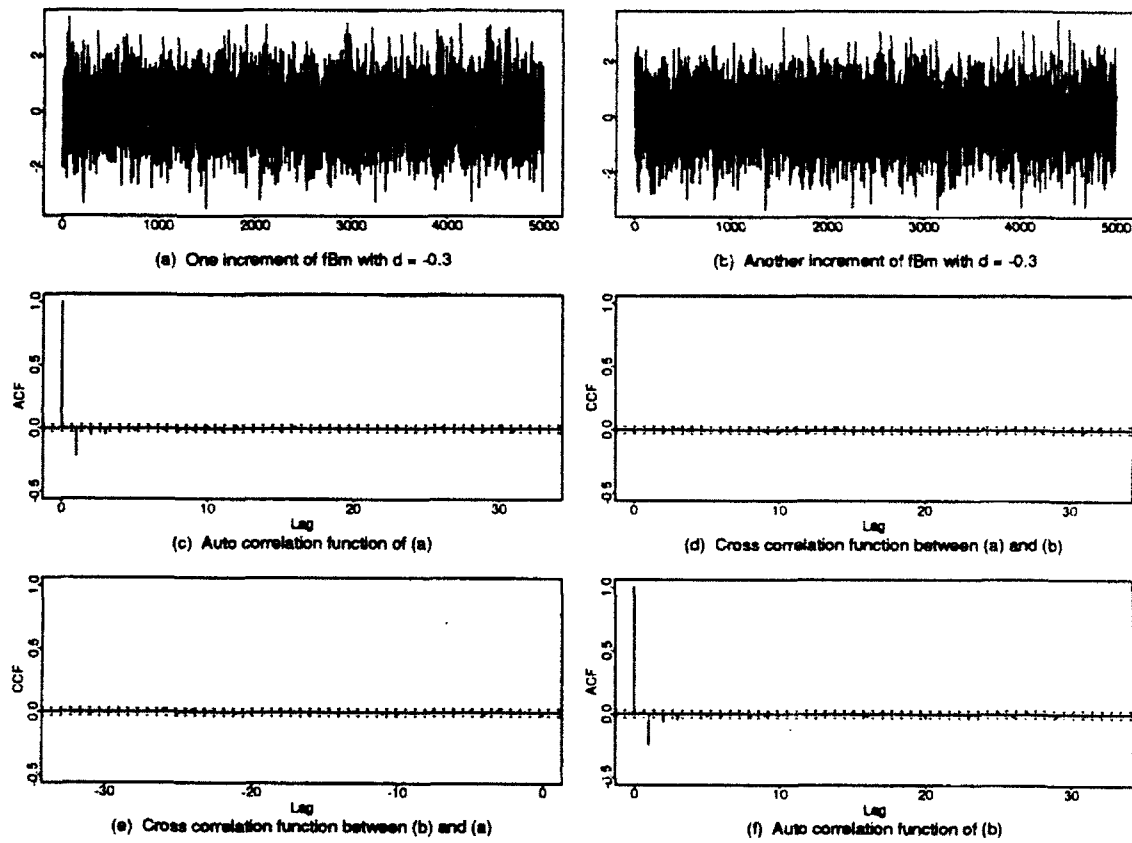


FIGURE 17. Correlation Functions Between Increments of fBm With $d = -0.3$.

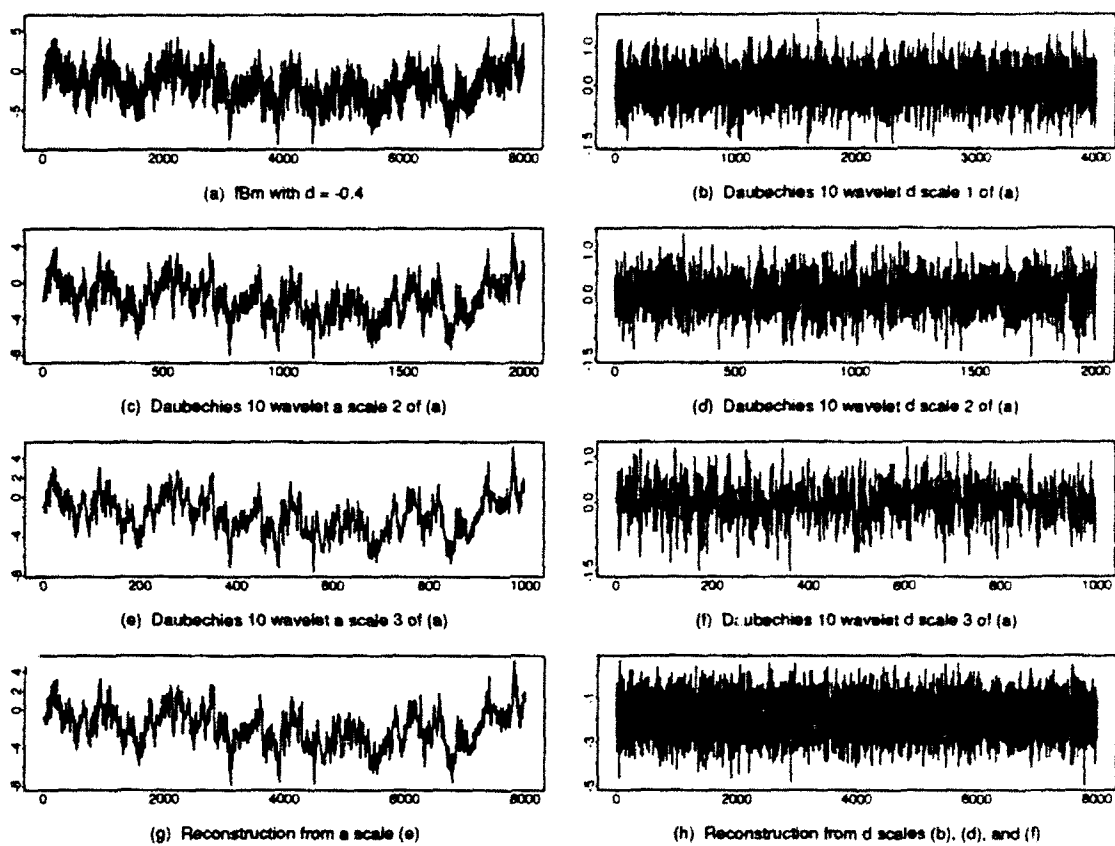


FIGURE 18. Decomposition and Reconstruction of fBm Using Daubechies 10 Wavelet.

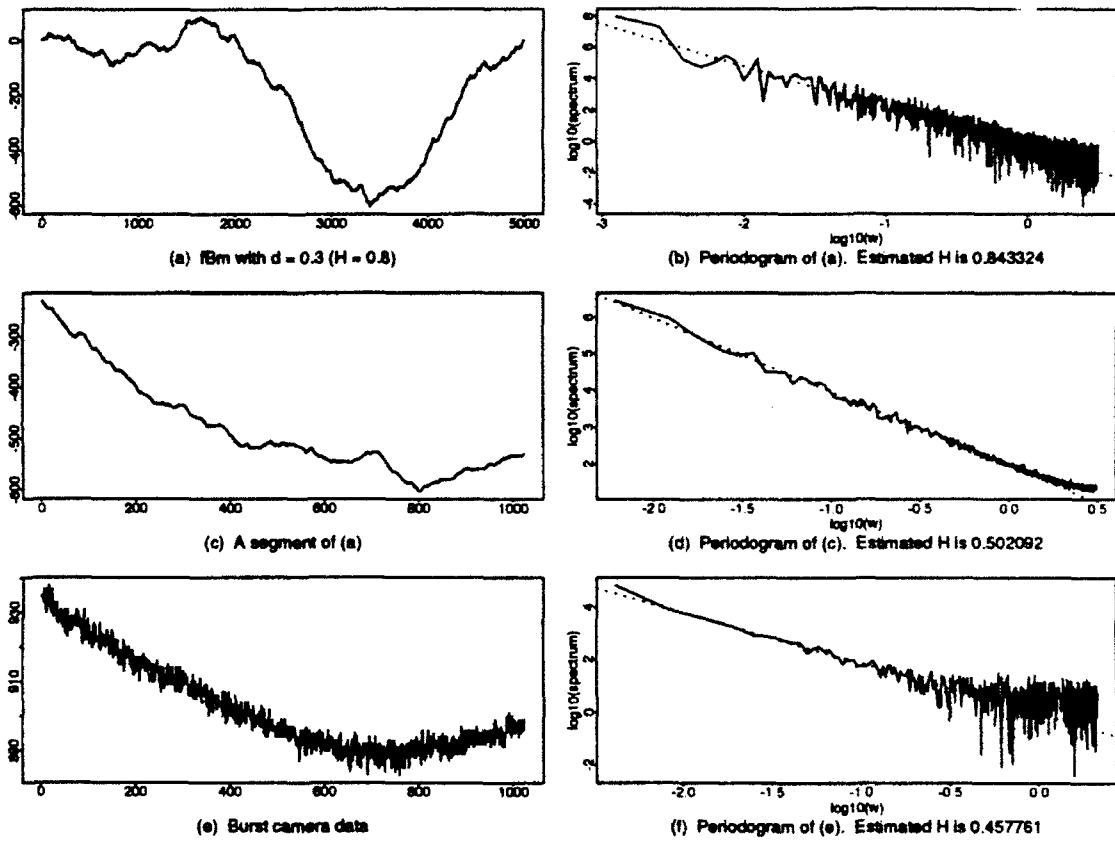


FIGURE 19. Comparison of the Estimated H for a Short-Term and a Long-Term fBm.

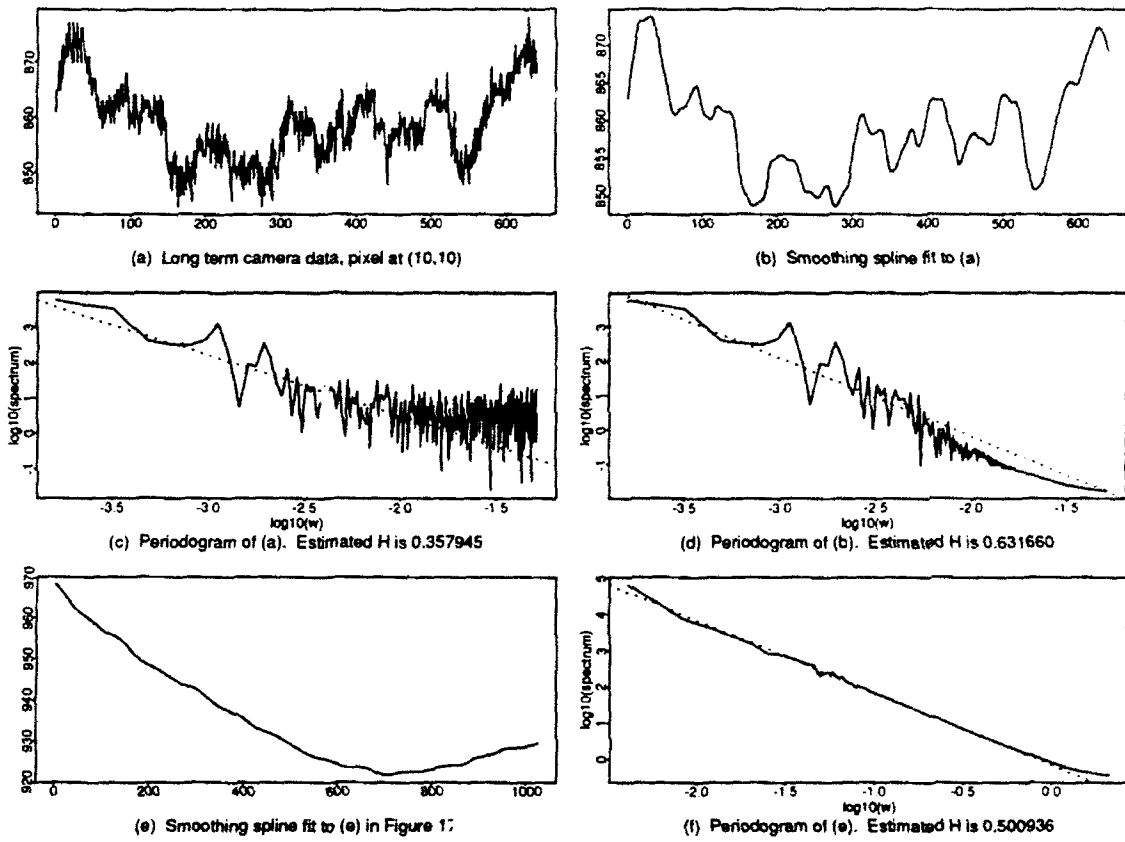


FIGURE 20. Power Spectrums for Amber Camera Data and Their Spline Fits.

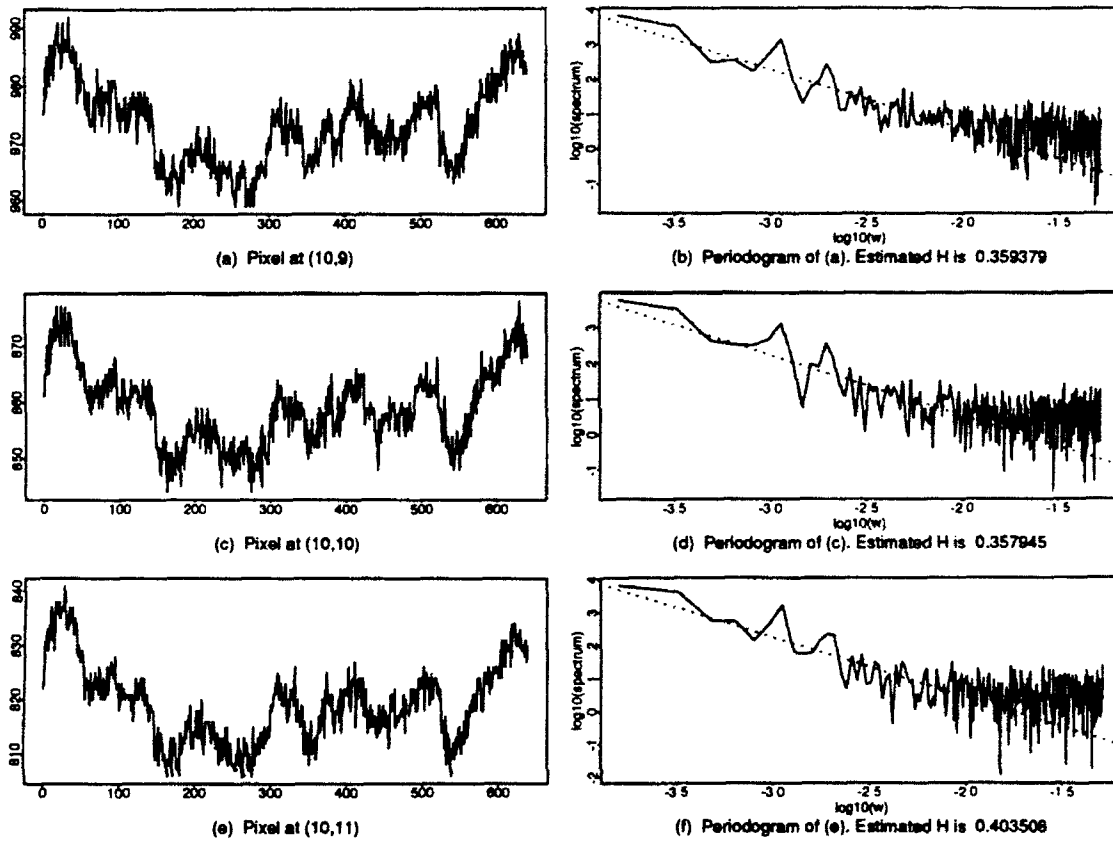


FIGURE 21. Long-Term Amber Camera Data and Their Periodograms.

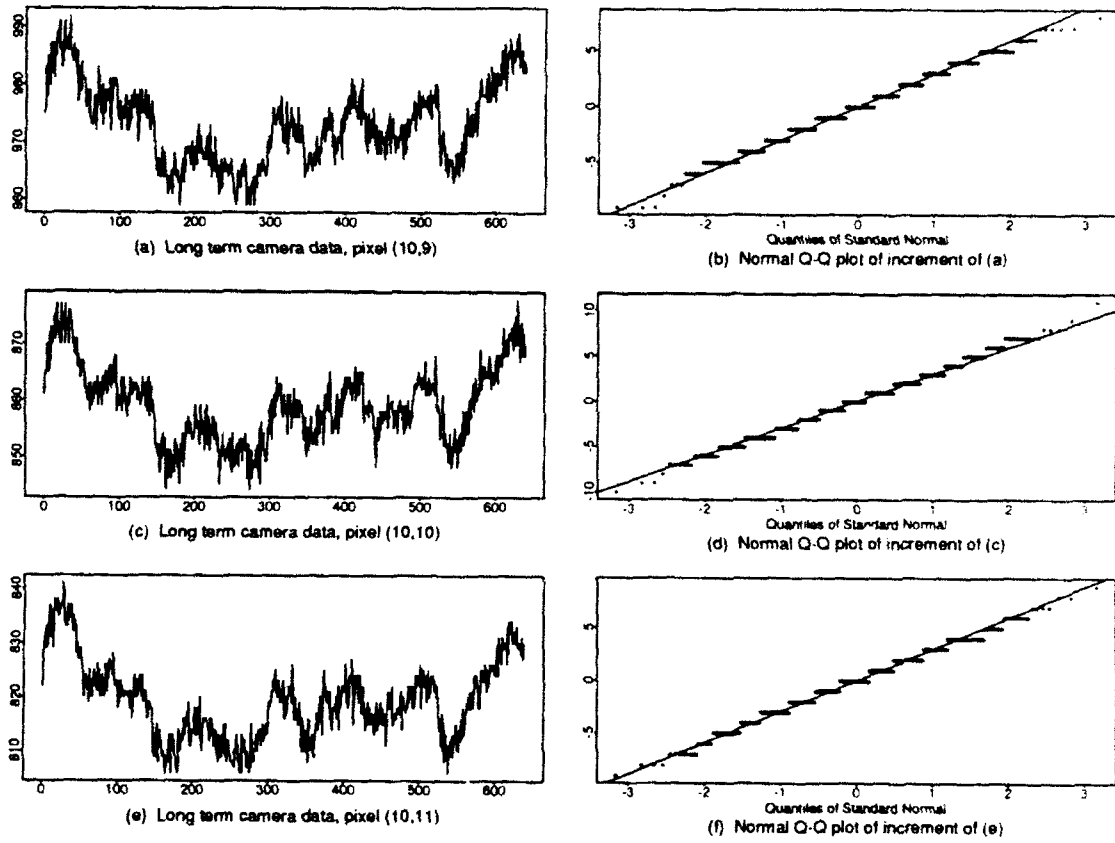


FIGURE 22. Amber Camera Data and Their Normal Q-Q Plots.

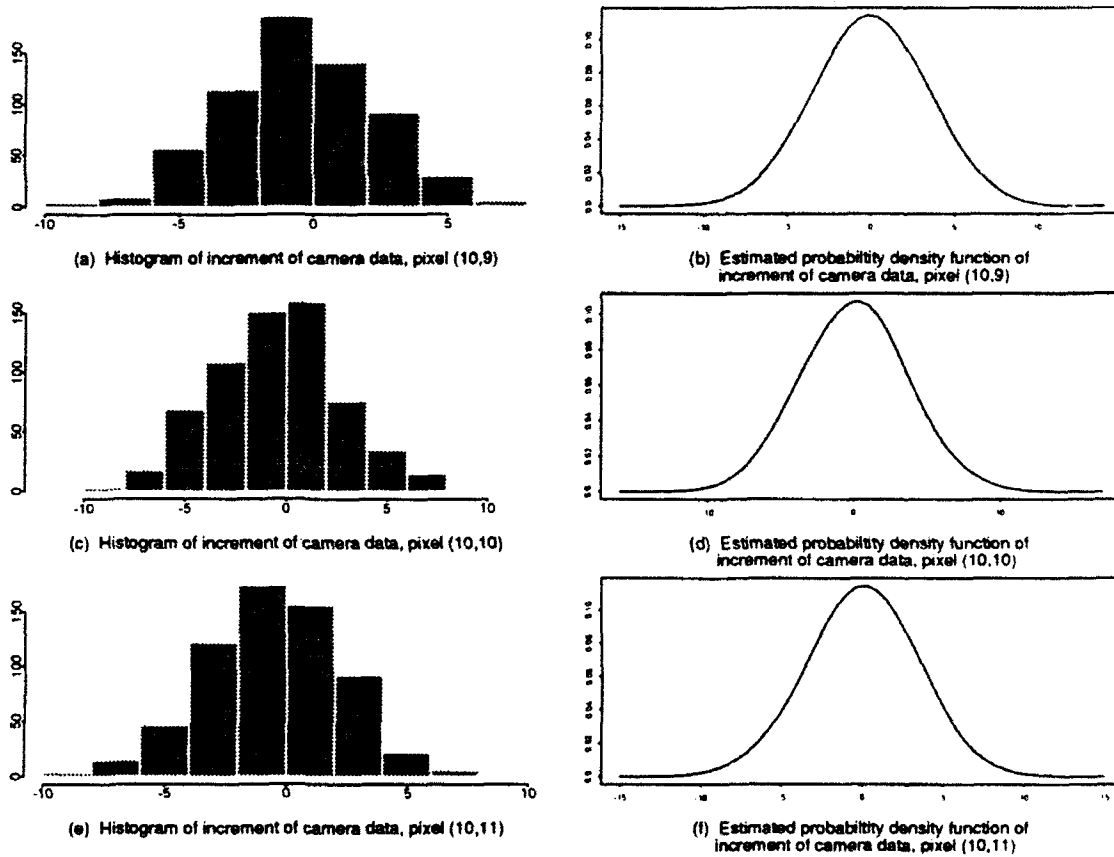


FIGURE 23. Histograms and Estimated Probability Density Functions of Long-Term Amber Camera Data.

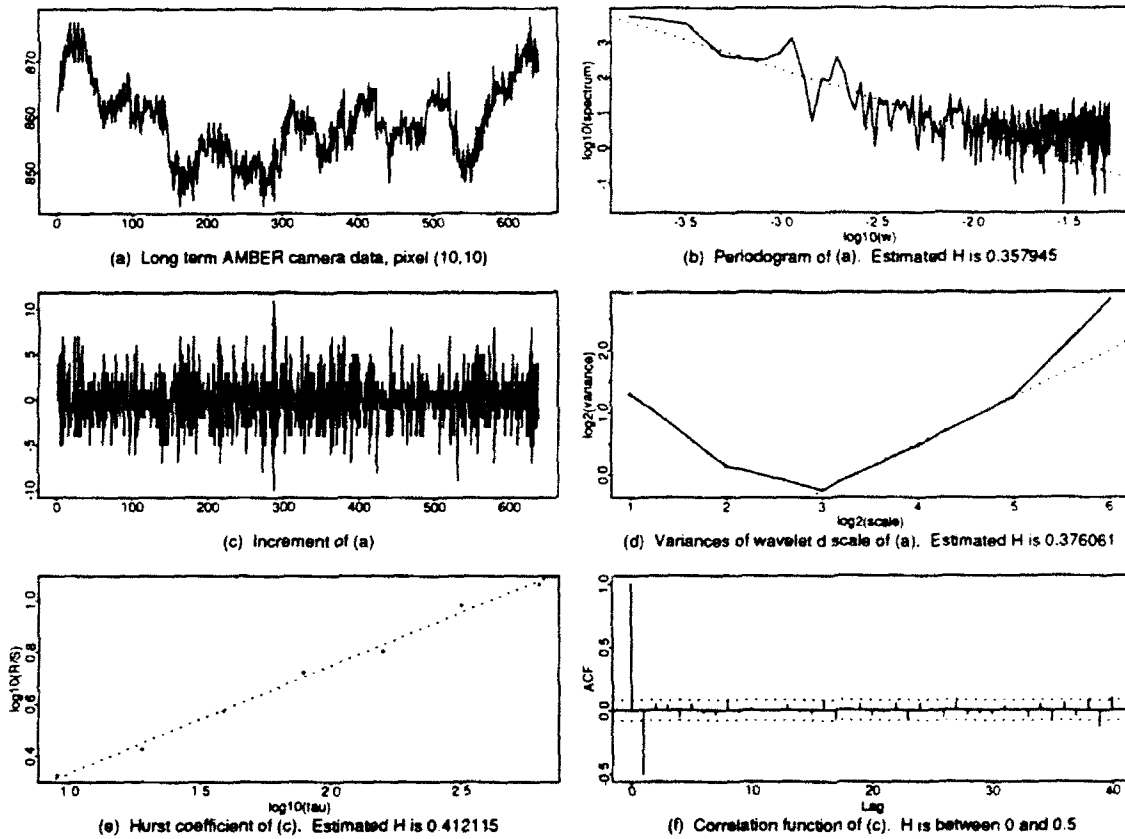


FIGURE 24. Comparison of the Estimated H for Long-Term Amber Camera Data.

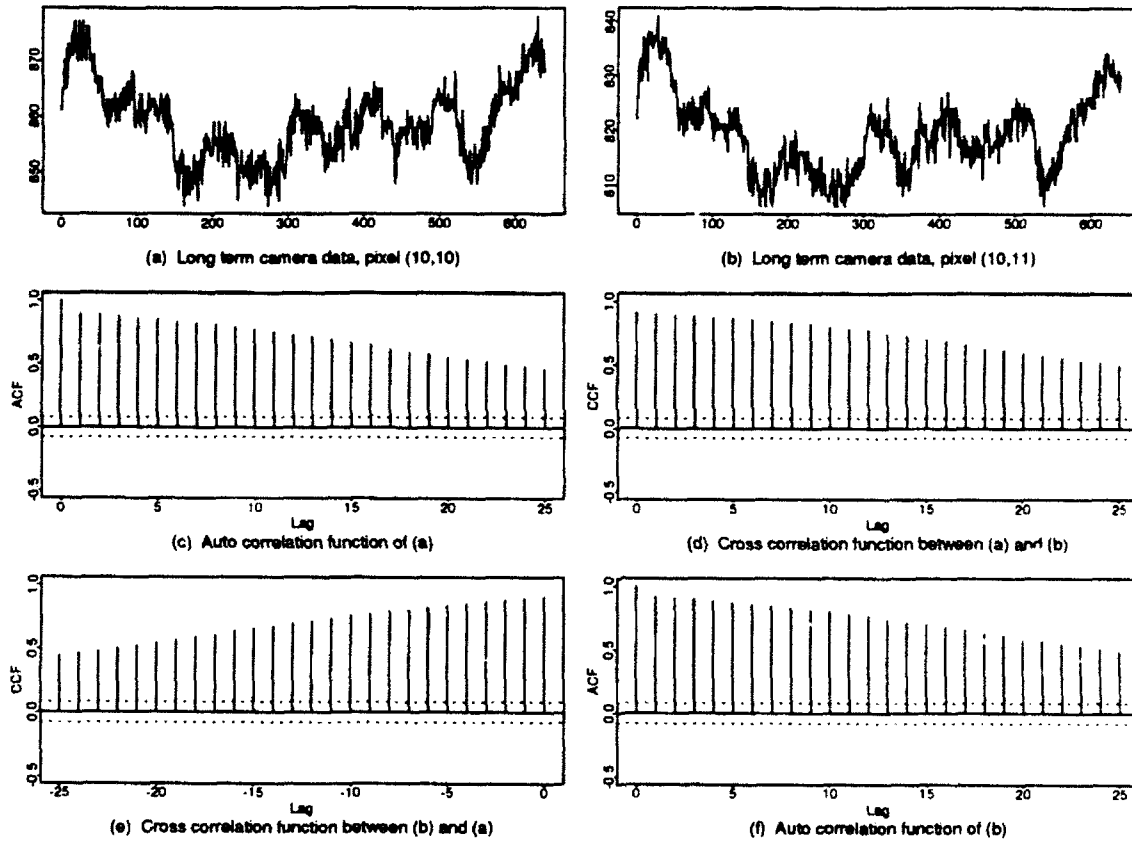


FIGURE 25. Correlation Functions Between Long-Term Amber Camera Data Pixel (10,10) and Pixel (10,11).

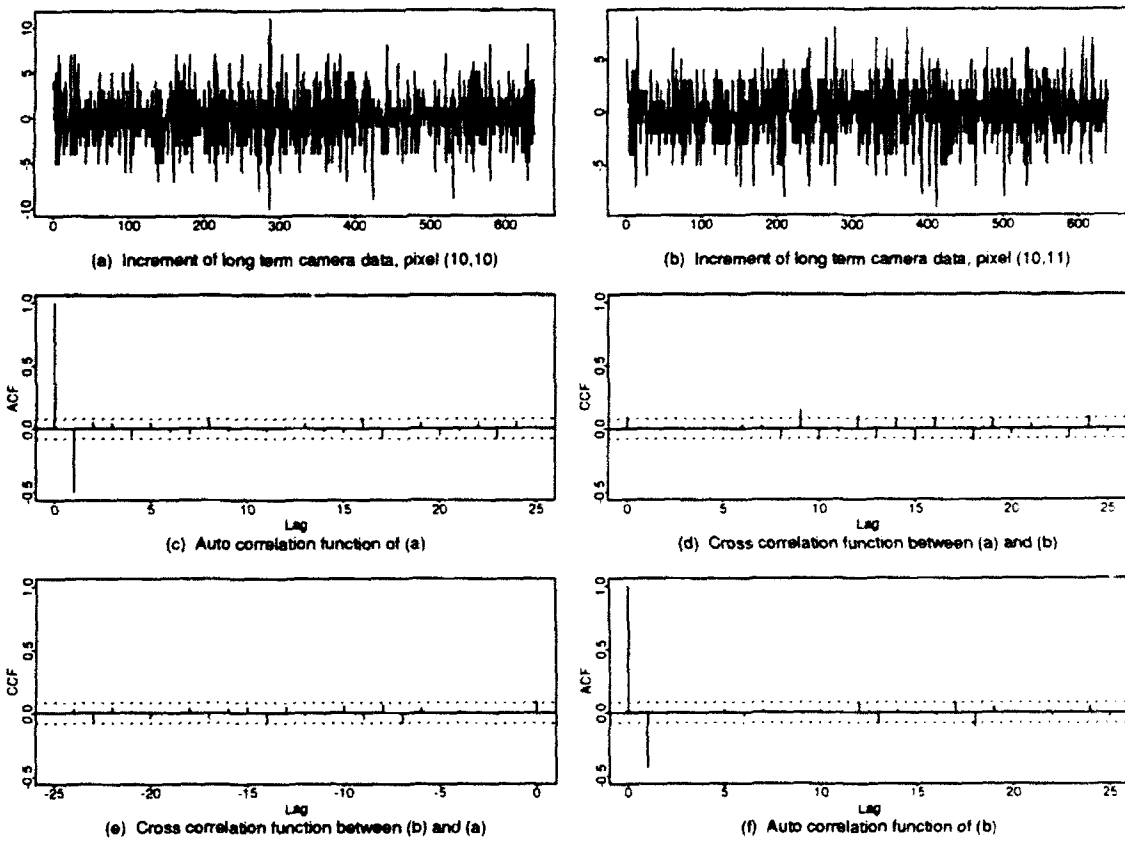


FIGURE 26. Correlation Functions Between Long-Term Amber Camera Data Pixel (10,10) and Pixel (10,11).

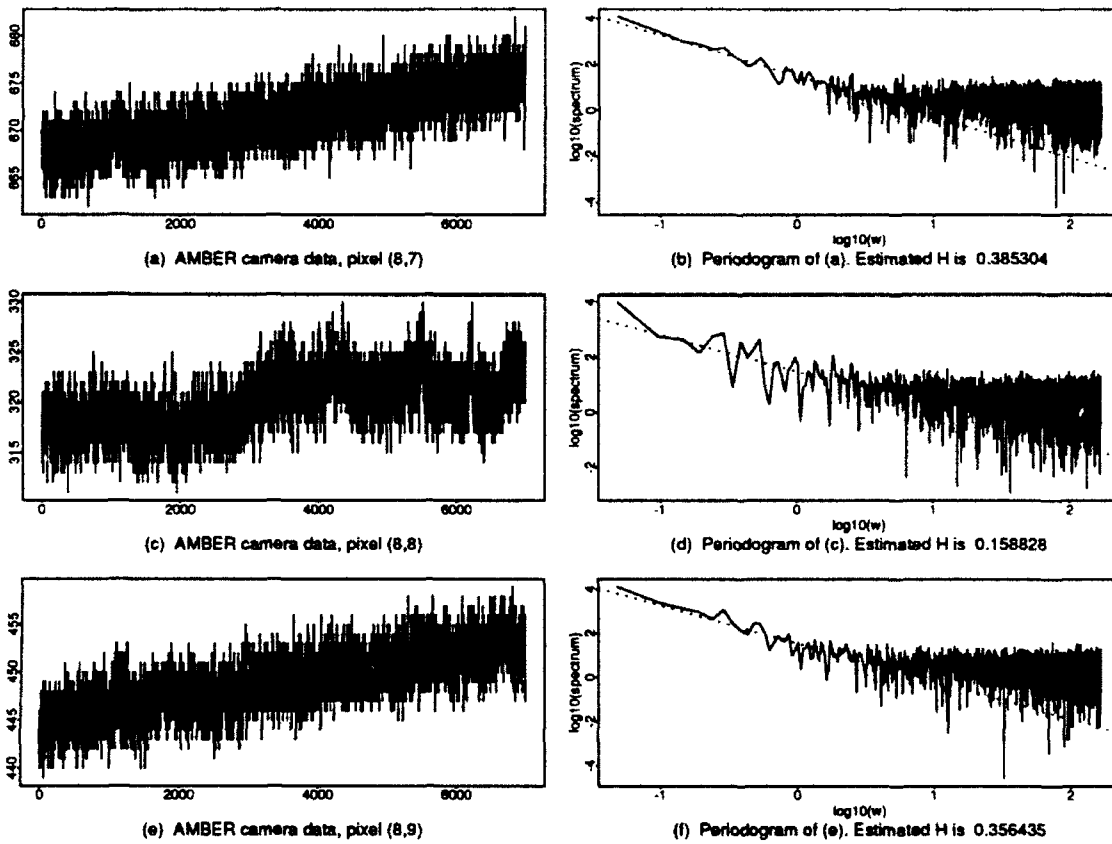


FIGURE 27. 54-Hertz Amber Camera Data and Their Periodograms.

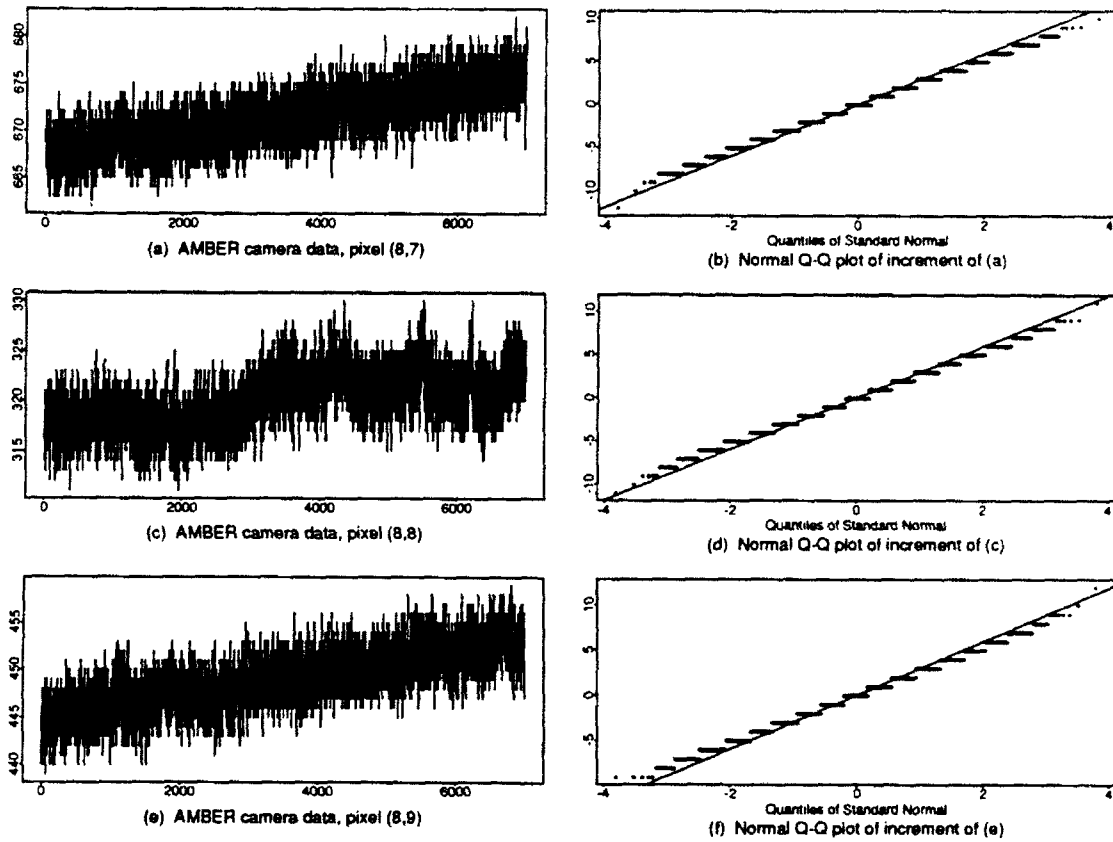


FIGURE 28. 54-Hertz Amber Camera Data and Their Normal Q-Q Plots.

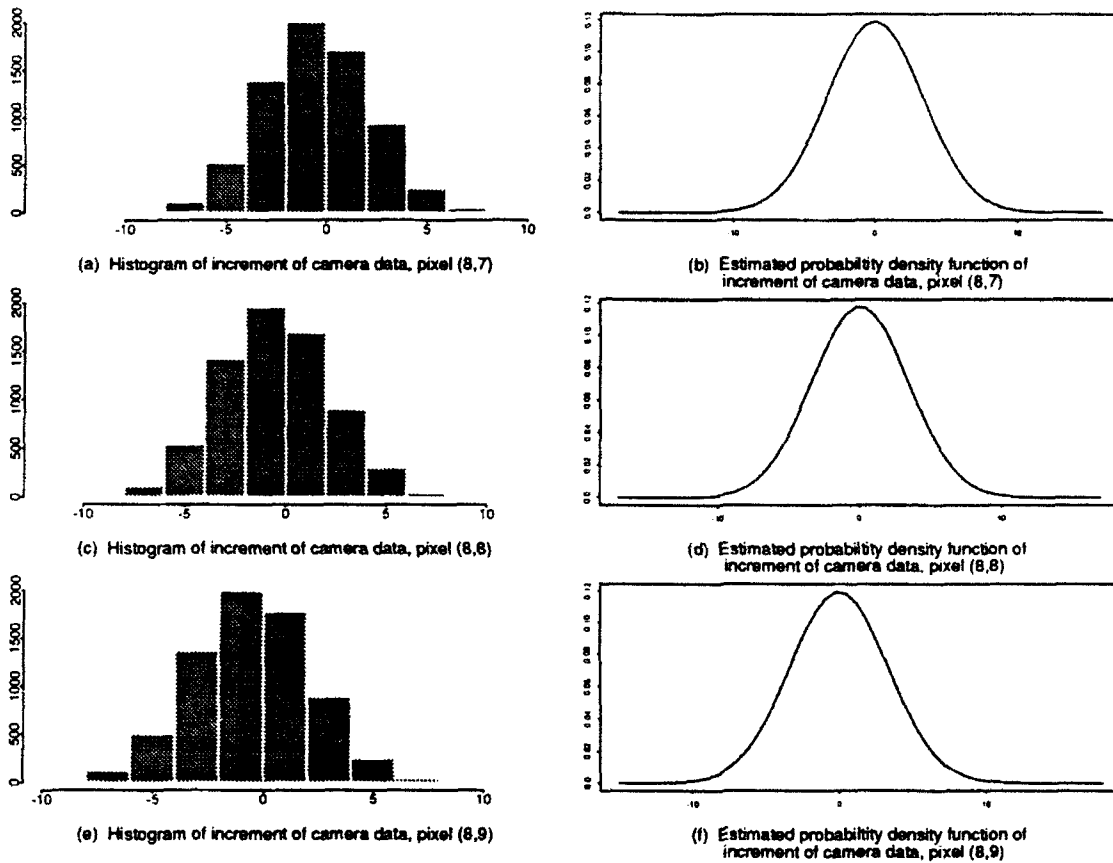


FIGURE 29. Histograms and Estimated Probability Density Functions of 54-Hertz Amber Camera Data.

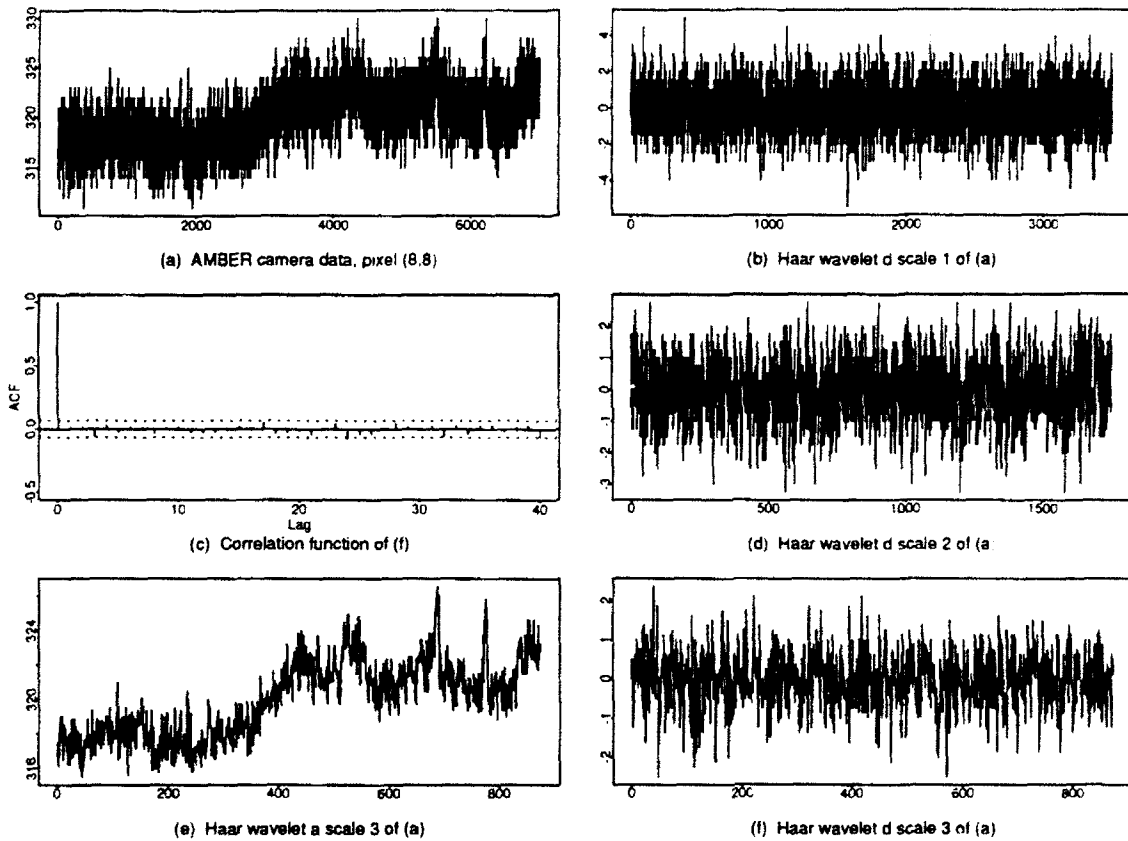


FIGURE 30. 54-Hertz Amber Camera Data and Haar Wavelet.

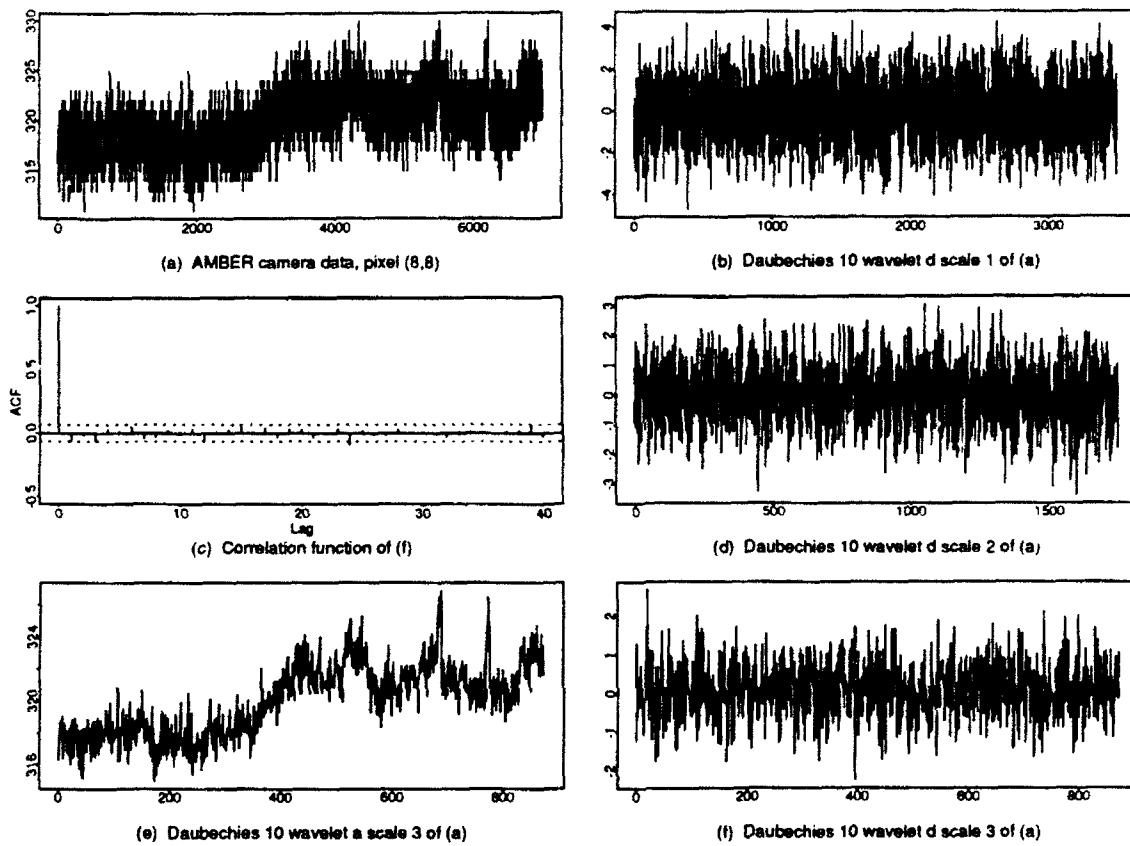


FIGURE 31. 54-Hertz Amber Camera Data and Daubechies 10 Wavelet.

REFERENCES

1. D. A. Scribner, K. A. Sarkady, M. R. Kruer, and J. C. Gridley. "Measurement, Characterization, and Modeling of Noise in Staring Focal Plane Arrays," *SPIE Infrared Sensors and Sensor Fusion*, Vol. 782 (1987), pp. 147-60.
2. D. A. Scribner, M. R. Kruer, and J. C. Gridley. "Physical Limitations to Nonuniformity Correction in IR Focal Plane Arrays," *SPIE Focal Plane Arrays: Technology and Applications*, Vol. 865 (1987), pp. 185-202.
3. D. A. Scribner, K. A. Sarkady, M. R. Kruer, and J. C. Gridley. "Test and Evaluation of Stability in IR Staring Focal Plane Arrays After Nonuniformity Correction," *SPIE Vol. 1108, Test and Evaluation of Infrared Detectors and Arrays* (1989), pp. 255-64.
4. D. A. Scribner, K. A. Sarkady, J. T. Caulfield, M. R. Kruer, G. Katz, J. C. Gridley, and Charles Herman. "Nonuniformity Correction for Staring IR Focal Plane Arrays Using Scene-Based Techniques," *SPIE Vol. 1308, Infrared Detectors and Focal Plane Arrays* (1990), pp. 224-33.
5. D. Wolf. "1/f Noise," in *Noise in Physical System*, D. Wolf, ed. Heidelberg, Springer, 1978, pp. 122-31.
6. Jerry Silverman, Jonathan Mooney, and Freeman Shephaerd. "Infrared Video Cameras," *Scientific American*, Vol. 266, No. 3 (1992), pp. 78-83.
7. B. J. West and M. F. Shlesinger. "On 1/f Noise and Other Distributions With Long Tails," *Proc. Natl. Acad. Sci.*, Vol. 79 (1982), pp. 3380-83.
8. E. W. Montroll and M. F. Shlesinger. "On the Ubiquity of 1/f Noise," *Int. J. Mod. Phys.*, Vol. 3 (1989), pp. 795-819.
9. Manfred Schroeder. *Fractals, Chaos, Power Laws*. New York, W. H. Freeman and Company, 1990.
10. Victor Solo. "Intrinsic Random Functions and the Paradox of 1/f Noise," *SIAM J. Appl. Math.*, Vol. 52, No. 1 (February 1992), pp. 270-91.
11. Gregory W. Wornell. "A Karhunen-Loeve Like Expansion for 1/f Processes Via Wavelets," *IEEE Trans. Inform. Theory*, Vol. IT-36 (1990), pp. 859-61.

12. Gregory W. Wornell. *Synthesis, Analysis, and Processing of Fractal Signals*. Cambridge, Mass., Research Laboratory of Electronics, Massachusetts Institute of Technology, No. 566 (October 1991).
13. Richard J. Barton and H. Vincent Poor. "Signal Detection in Fractional Gaussian Noise," *IEEE Trans. on Information Theory*, Vol. 34 (1988), pp. 943-59.
14. J. R. M. Hosking. "Modeling Persistence in Hydrological Time Series Using Fractional Differencing," *Water Resources Research*, Vol. 20 (1984), pp. 1898-1908.
15. Emanuel Parzen. *Stochastic Processes*. San Francisco, Holden-Day, 1962.
16. Athanasios Papoulis. *Probability, Random Variables, and Stochastic Processes*. San Francisco, McGraw-Hill Book Company, 1965.
17. Alan V. Oppenheim and Ronald W. Schaffer. *Digital Signal Processing*. New York, Prentice Hall, Inc., 1975.
18. Benoit Mandelbrot and John W. Van Ness. "Fractional Brownian Motions, Fractional Noises and Applications," *SIAM Review*, Vol. 10, No. 2 (1988), pp. 422-37.
19. Jens Feder, *Fractals*. San Francisco, Plenum Press, 1988.
20. Benoit Mandelbrot. *The Fractal Geometry of Nature*. San Francisco, Freeman, 1982.
21. J. Ramanathan and O. Zxeitouni. "On the Wavelet Transform of Fractional Brownian Motion," *IEEE Trans. Inform. Theory*, Vol. IT-37 (1991), pp. 1156-58.
22. P. Flandrin. "On the Spectrum of Fractional Brownian Noise," *IEEE Trans. on Information Theory*, Vol. 36 (1989), pp. 197-99.
23. -----, "Wavelet Analysis and Synthesis of Fractional Brownian Noise," *IEEE Trans. on Information Theory*, Vol. 38 (1992), pp. 910-16.
24. Ingrid Daubechies. "Orthonormal Bases of Wavelets with Compact Support," *Comm. Pure Appl. Math.*, Vol. 41 (1988), pp. 909-996.
25. -----, *Ten Lectures on Wavelets*. CBSM-NSF Regional Conference Series in Applied Mathematics, Vol. 60. Philadelphia, Pa., Society for Industrial and Applied Mathematics, 1992.
26. A. Grossman and J. Morlet. "Decomposition of Hardy Functions Into Square Integrable Wavelets of Constant Shape," *SIAM J. Math, Anal.*, Vol. 15 (1984), pp. 723-36.

27. S. G. Mallat. "A Theory for Multiresolution Signal Decomposition: The Wavelet Representation," *IEEE Trans. Pattern Anal. Machine Intell.*, Vol. 11 (1989), pp. 674-93.
28. Naval Ocean Systems Center. *The Discrete Wavelet Transform*, by M. J. Shensa. San Diego, Calif., NOSC, 1991. (NOSC Technical Report 1426, publication UNCLASSIFIED.)
29. H. Zou and A. H. Tewfik. "A Theory of M-Band Orthogonal Wavelets," submitted to *IEEE Trans. on Circuits and Systems*.
30. A. Cohen and I. Daubechies. "Orthonormal Bases of Comapctly Supported Wavelets—III. Better Frequency Resolution" (in process).
31. A. H. Tewfik and M. Kim. "Correlation Structure of the Discrete Wavelet Coefficients of Fractional Brownian Motion ," *IEEE Trans. on Information Theory*, Vol. 38 (1992), pp. 904-09.
32. S. G. Mallat and S. Zhong. "Characteristics of Signals From Multiscale Edges," to appear *IEEE Trans. Pattern Anal. Machine Intell.*
33. J. R. M. Hosking. "Fractional Differencing," *Biometrika*, Vol. 68 (1981), pp. 165-76.
34. C. W. J. Granger and Roselyne Joyeux. "An Introduction to Long-Memory Time Series Models and Fractional Differencing," *Journal of Time Series Analysis*, Vol. 1 (1998), pp.15-29.
35. John Haslett and Adrian E. Raftery. "Space-Time Modelling with Long-memory Dependence: Assessing Ireland's Wind Power Resource," *Appl. Statist.*, Vol. 38 (1989), pp. 1-50.
36. M. Deriche and A. H. Tewfik. " Maximum Likelihood Estimation of the Parameters of Discrete Fractionally Differenced Gaussian Noise Process," submitted to *IEEE Trans. on Signal Processing*, August 1991.
37. R. Gnanadesikan. *Methods for Statistical Data Analysis of Multivariable Observations*. New York, John Wiley & Sons, 1977.
38. Massachusetts Institute of Technology. *A Stochastic Modelling Approach to Multiscale Signal Processing*, by Kenneth Chien-ko Chou. Cambridge, Mass., MIT, Laboratory for Information and Decision Systems, May 1991. (LIDS-TH-2036, publication UNCLASSIFIED.)

INITIAL DISTRIBUTION

- 1 Naval Air Systems Command (AIR-540TH, R. Habayeb)
- 6 Chief of Naval Research, Arlington
 - ONCR-223, D. Siegel (1)
 - OCNR-1111
 - Dr. J. Abrahams (1)
 - Dr. N. Gere (1)
 - OCNR-1112, Dr. M. Schlesinger (1)
 - OCNR-1264, W. J. Miceli (1)
 - Dr. K. NG (1)
- 1 Office of Naval Research Europe (Dr. R. Ryan)
- 2 Naval Command Control and Ocean Surveillance Center, RDT&E Division, San Diego
 - Code 632, Dr. M. Shensa (1)
 - Code 7601T, Dr. K. Bromley (1)
- 1 Naval Postgraduate School, Monterey (Code EC/GL, Prof. G. S. Gill)
- 3 Naval Research Laboratory
 - Code 5652
 - Dr. J. Caufleid (1)
 - Dr. D. Schribner (1)
 - Code 6552, Dr. M. Krueer (1)
- 1 Naval Surface Warfare Center Division, Dahlgren (Code G03-DLB, Brunson)
- 1 Naval Surface Warfare Center, Dahlgren Division Detachment White Oak, Silver Spring
 - Dr. P. Carter (1)
 - Dr. R. Cawley (1)
- 1 Army Missile Command, Redstone Arsenal (AMSMI-RD-GC, Dr. P. Jacobs)
- 1 Air Force Wright Laboratory, Armament Directorate, Eglin Air Force Base (M. F. wehling)
- 1 Defense Advanced Research Projects Agency, Arlington (LTCOL J. Crowley)
- 2 Defense Technical Information Center, Alexandria
- 3 Massachusetts Institute of Technology, Lincoln Laboratory, Lexington, MA
 - Dr. T. Nguyen (1)
 - Prof. A. Willsky (1)
 - Dr. G. W. Wornell (1)
- 1 New York University, Courant Institute of Mathematical Sciences, New York, NY (Prof. S. Mallat)
- 1 Pennsylvania State University, Applied Research Laboratory, State College, PA (Dr. Jack Hansen)
- 1 Statistical Sciences, Incorporated, Seattle, WA (Dr. R. D. Martin)
- 1 University of California, Electrical and Computer Science Department, Santa Barbara, CA (Dr. C. Kenney)
- 1 University of Minnesota, Department of Electrical Engineering, Minneapolis, MN (Dr. A. H. Tewfik)